



MANEUVER ESTIMATION MODEL FOR RELATIVE ORBIT DETERMINATION

THESIS

Tara R. Storch, Capt, USAF

AFIT/GA/ENY/05-M011

DEPARTMENT OF THE AIR FORCE  
AIR UNIVERSITY

**AIR FORCE INSTITUTE OF TECHNOLOGY**

Wright-Patterson Air Force Base, Ohio

APPROVED FOR PUBLIC RELEASE; DISTRIBUTION UNLIMITED.

The views expressed in this thesis are those of the author and do not reflect the official policy or position of the United States Air Force, Department of Defense, or the United States Government.

AFIT/GA/ENY/05-M011

MANEUVER ESTIMATION MODEL FOR RELATIVE ORBIT  
DETERMINATION

THESIS

Presented to the Faculty

Department of Aeronautics and Astronautics

Graduate School of Engineering and Management

Air Force Institute of Technology

Air University

Air Education and Training Command

In Partial Fulfillment of the Requirements for the  
Degree of Master of Science in Astronautical Engineering

Tara R. Storch, B.S.

Capt, USAF

March, 2005

APPROVED FOR PUBLIC RELEASE; DISTRIBUTION UNLIMITED.

MANEUVER ESTIMATION MODEL FOR RELATIVE ORBIT  
DETERMINATION

Tara R. Storch, B.S.  
Capt, USAF

Approved:

/signed/

21 Mar 2005

---

Dr. William E. Wiesel  
Advisor

---

date

/signed/

21 Mar 2005

---

Lt Col Kerry D. Hicks  
Committee Member

---

date

/signed/

21 Mar 2005

---

Lt Col Nathan A. Titus  
Committee Member

---

date

## *Abstract*

While the use of relative orbit determination has made in reducing minimizing the difficulties inherent in tracking geostationary satellites that are in close proximity, the problem is often compounded by stationkeeping operations or unexpected maneuvers. If a maneuver occurs, observations will no longer fit predicted data, increasing the risk of misidentification and cross-tagging.

The goal of this research was to develop a model that will estimate the magnitude, direction, and time of a suspected maneuver performed by a collocated geostationary satellite. Relative motion was modelled using Hill's equations, and least squares estimation was employed to create both a linear non-maneuver model and non-linear maneuver model. Two sets of data for an actual satellite collocation were obtained from the Air Force Maui Optical and Supercomputing (AMOS) site, consisting of differential right ascension and declination. Studies conducted with these observations, along with simulation studies, indicate that it is indeed possible to perform maneuver estimation. It was found, however, that the amount of data required for successful convergence is much greater than that typically obtained for tracking purposes.

## *Acknowledgements*

All praise and glory to my God and King. I thank You, Lord, for all the blessings You have given me. Thank You for this opportunity, for the wonderful classmates, instructors, and friends to help me along, for bringing me through this program, and most of all for using this time at AFIT to teach me about so much more than astro.

I would like to thank my advisor, Dr. William Wiesel, for his willingness to impart knowledge and for his enduring patience in the process. I am truly thankful to have had the opportunity to work with him. Thanks to my sponsor, Dr. Chris Sabol, for not only his time and efforts, but also for his intensity and high expectations.

I would also like to thank my church family for giving me a home away from home, for their prayers and for challenging me to grow in my faith. And as always, I am indebted to my wonderful family. Thanks to my sister and her family, and my brother for all the laughter, prayers, and support. And finally, special thanks goes to my parents for their unyielding love, encouragement, and faithful prayers during this season of my life.

Tara R. Storch

## *Table of Contents*

	Page
Abstract . . . . .	iv
Acknowledgements . . . . .	v
List of Figures . . . . .	viii
List of Tables . . . . .	ix
List of Symbols . . . . .	x
List of Abbreviations . . . . .	xi
 I. Introduction . . . . .	 1-1
1.1 Background . . . . .	1-1
1.2 Problem Statement . . . . .	1-2
1.3 Method of Solution . . . . .	1-2
 II. Literature Review . . . . .	 2-1
2.1 Optical Observations . . . . .	2-1
2.1.1 Fundamentals - Celestial Sphere Geometry . . .	2-1
2.1.2 The Raven Telescope . . . . .	2-2
2.1.3 Topocentric to Geocentric Conversion . . . . .	2-3
2.2 Least Squares Estimation . . . . .	2-4
2.2.1 The Principle of Maximum Likelihood . . . . .	2-5
2.2.2 Linearized Dynamics and the State Transition Ma- trix . . . . .	2-5
2.2.3 Linear Least Squares . . . . .	2-7
2.2.4 Nonlinear Least Squares . . . . .	2-9
2.3 Relative Motion . . . . .	2-11
2.3.1 Equations of Motion . . . . .	2-11
2.3.2 Differential Orbital Element Effects . . . . .	2-11
2.4 Relative Motion Applications in GEO . . . . .	2-12
2.4.1 GEO Clusters . . . . .	2-12
2.4.2 Close Approaches . . . . .	2-14
2.5 Chapter Outline . . . . .	2-15

	Page
III. Methodology . . . . .	3-1
3.1 Coordinate Transformation . . . . .	3-1
3.2 The Observation Function and Its Linearization . . . . .	3-2
3.3 Linear System Dynamics . . . . .	3-7
3.4 The Maneuver Model: Non-linear System Dynamics . . . . .	3-9
3.5 Algorithm . . . . .	3-12
3.5.1 Data Files . . . . .	3-12
3.5.2 Initializing the State Vector . . . . .	3-13
3.5.3 Reference Orbit . . . . .	3-14
3.5.4 Least Squares Algorithm . . . . .	3-14
IV. Simulations and Real Data . . . . .	4-1
4.1 Relative Orbit Determination Experiment . . . . .	4-1
4.2 Simulation Study . . . . .	4-2
4.2.1 Non-maneuver Model Initial Simulation . . . . .	4-2
4.2.2 Maneuver Model Initial Simulation . . . . .	4-3
4.3 Raven Data – 2003 . . . . .	4-10
4.3.1 Data Set 1: 29 – 31 July . . . . .	4-11
4.3.2 Data Set 2: 30 July - 1 August . . . . .	4-17
4.4 Raven Data - 2004 . . . . .	4-19
4.4.1 Data Set 1: 3 – 4 June . . . . .	4-20
4.4.2 Data Set 2: 4 – 5 June . . . . .	4-24
V. Conclusions . . . . .	5-1
5.1 Summary . . . . .	5-1
5.2 Conclusions . . . . .	5-1
5.2.1 Observability . . . . .	5-1
5.2.2 Higher Order Error Sources . . . . .	5-2
5.2.3 Sequential Maneuvers . . . . .	5-2
5.3 Future Work . . . . .	5-2
Bibliography . . . . .	4



## *List of Figures*

Figure		Page
2.1.	Geometry of the Celestial Sphere . . . . .	2-1
2.2.	Raven Image . . . . .	2-3
3.1.	Geocentric Inertial Frame . . . . .	3-2
3.2.	Body Fixed Frame . . . . .	3-3
3.3.	Maneuver Dynamics . . . . .	3-10
4.1.	COWPOKE and TLE predictions for observations on 30,31 July	4-1
4.2.	Fit to 30 <sup>th</sup> and 31 <sup>st</sup> , Predict to 1 <sup>st</sup> . . . . .	4-2
4.3.	Estimated and Simulated Observations . . . . .	4-4
4.4.	Non-maneuver Fit to 29 – 31 July . . . . .	4-11
4.5.	Non-maneuver Fit to 29 – 31 July . . . . .	4-12
4.6.	Maneuver Fit to 29 – 31 July, $t_m = 79477$ . . . . .	4-14
4.7.	RA vs Dec for 29 – 31 July, $t_m = 79477$ . . . . .	4-15
4.8.	Maneuver Fit to 29 – 31 July, $t_m = 125340$ . . . . .	4-15
4.9.	RA vs Dec for 29 – 31 July, $t_m = 125340$ . . . . .	4-16
4.10.	Maneuver Fit to 29 – 31 July, $t_m = 168380$ . . . . .	4-17
4.11.	RA vs Dec for 29 – 31 July, $t_m = 168380$ . . . . .	4-18
4.12.	Non-maneuver Fit to 31 July - 1 August . . . . .	4-19
4.13.	Non-maneuver Fit to 3-4 June . . . . .	4-22
4.14.	Non-maneuver RA vs Dec for 3-4 June . . . . .	4-22
4.15.	Maneuver Fit to 3 – 4 June, $t_m = 80008$ . . . . .	4-23
4.16.	RA vs Dec for 3 – 4 June, $t_m = 80008$ . . . . .	4-23
4.17.	RA vs Dec Solution for 3 – 4 June Propagated to 5 June . . .	4-24
4.18.	Maneuver Fit to 4 – 5 June, $t_m = 87311$ . . . . .	4-25
4.19.	RA vs Dec for 4 – 5 June, $t_m = 87311$ . . . . .	4-26

# *List of Tables*

Table		Page
4.1.	Data Arc Time and Length for 29 July - 1 August . . . . .	4-5
4.2.	Simulated Data Arc Time and Length . . . . .	4-6
4.3.	Convergence Times and Values for Simulated Data Arcs . . . . .	4-7
4.4.	State Vector Solution for Convergence Times . . . . .	4-8
4.5.	State Vector Solution for Convergence Times . . . . .	4-9
4.6.	State Vector Solution for No Maneuver Data Set in Maneuver Model . . . . .	4-10
4.7.	State Vector Solution for Non-maneuver Fit to 29 – 31 July . . . . .	4-11
4.8.	Convergence Times and Values for 29-31 July . . . . .	4-13
4.9.	State Vector Solution for Maneuver Fit to 29 – 31 July . . . . .	4-13
4.10.	State Vector Solution for Non-maneuver Fit to 30 July - 1 August . . . . .	4-18
4.11.	Data Arc Time and Length for 3 June . . . . .	4-20
4.12.	State Vector Solution for Maneuver Fit to 3-4 June . . . . .	4-21
4.13.	State Vector Solution for Maneuver Fit to 4-5 June . . . . .	4-25

# *List of Symbols*

Symbol		Page
$\alpha$	right ascension . . . . .	2-4
$d$	declination . . . . .	2-4
$a$	semimajor axis . . . . .	2-12
$i$	inclination . . . . .	2-12
$\Omega$	right ascension of the ascending node . . . . .	2-12
$M$	mean anomaly . . . . .	2-12
$\omega$	argument of perigee . . . . .	2-12
$u$	argument of latitude . . . . .	3-1
$r_{rms}$	root mean square of the residuals . . . . .	4-3

*List of Abbreviations*

Abbreviation		Page
GEO	Geosynchronous Orbit . . . . .	1-1
AMOS	Air Force Maui Optical and Supercomputing site . . . . .	1-2
CCD	Charge-Coupled Device . . . . .	2-2
COWPOKE	Cluster Orbits With Perturbations Of Keplerian Elements	2-11
TLE	Two-Line Element set . . . . .	3-14

# MANEUVER ESTIMATION MODEL FOR RELATIVE ORBIT DETERMINATION

## I. Introduction

### 1.1 *Background*

The concept of the geosynchronous orbit, and its more specific counterpart, the geostationary orbit, has been around for more than a century. While Arthur C. Clark became widely known for this concept in October of 1945, it was first proposed in the early 1900's by Russian theorist Konstantin Tsiolkovsky. This concept became a reality in July of 1963, when Syncom 2 became the first operational geosynchronous communications satellite [7].

Since then, the geosynchronous orbit (GEO) regime has proven to be an invaluable asset, so much so that the number of satellites placed in these orbits has risen dramatically. While demand for this capability continues to increase, the available number of orbital slot allocations continues to decrease. Consequently, many organizations are choosing to collocate satellites in the same slot. In addition to intentional collocation, cases now exist where satellites unwittingly have been placed in a position where one stationkeeping box overlaps another, leading to an increased vulnerability of unintentional close approaches [4]. And of course, as in any orbital regime, an increase in space debris and malfunctioning vehicles lead to another potential for close approaches and collisions.

Whether intentional or unintentional, collocation and close approaches increase the difficulty of identifying individual satellites within clusters and create the potential for misidentification and cross-tagging. While various identification methods exist, increased orbit determination accuracy is a valuable way to monitor the extent of close approaches, thus minimizing the need for expensive precautionary collision avoidance maneuvers. Relative motion has emerged as a potential asset in supplying spacecraft

identification information. By using relative metric data from optical sensors and relative equations of motion, spacecraft separations can be estimated and predicted [5].

### ***1.2 Problem Statement***

While relative orbit determination has made improvements in minimizing the inherent difficulties in tracking objects in close proximity, the problem is often compounded by stationkeeping operations or unexpected maneuvers performed by one or more satellites. If a maneuver takes place, the observations will no longer fit the predicted data and misidentification and cross tagging are problems once again.

### ***1.3 Method of Solution***

The goal of this research is to create a model that will estimate the magnitude, direction, and time of a suspected maneuver performed by a collocated satellite. Relative orbit determination and least squares estimation are employed to create both a linear non-maneuver model and non-linear maneuver model. Observations, obtained from the Air Force Maui Optical and Supercomputing (AMOS) site, consist of differential right ascension and declination, and dynamics will be modelled using Hill's equations.

## II. Literature Review

### 2.1 Optical Observations

#### 2.1.1 Fundamentals - Celestial Sphere Geometry. [8,15]

Most celestial objects observed from Earth are at a distance many times greater than that of the earth's radius, giving each an apparent fixed position on the inner surface of a celestial sphere. This discussion then, will begin with definitions associated with the celestial sphere, see Figure 2.1.

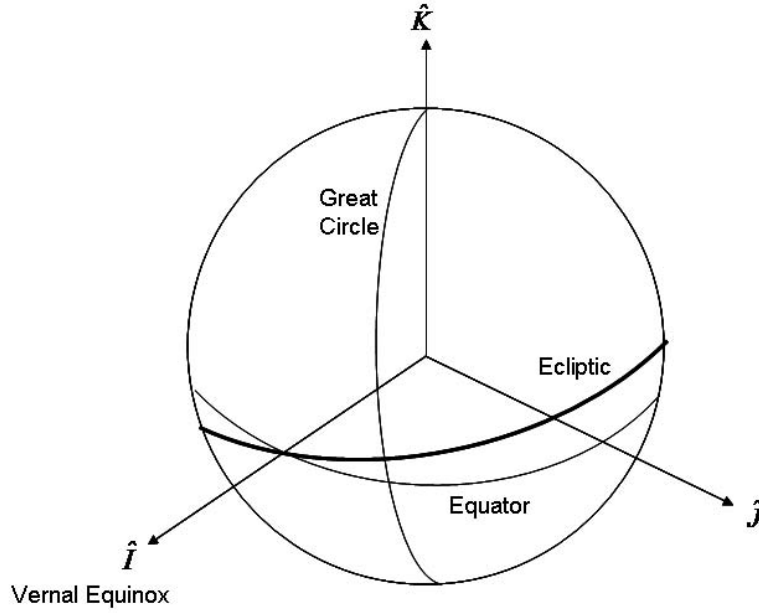


Figure 2.1: Geometry of the Celestial Sphere

The celestial equator is the plane passing through the earth's equator which intersects the celestial sphere. The celestial poles are defined as the intersection of the celestial sphere with the rotation axes of the earth, both north and south. A great circle is the intersection of the celestial sphere with any plane passing through the center of the sphere. An hour circle is one such great circle. Hour circles are defined as great circles that pass through the celestial poles and are thus perpendicular to the celestial equator.

Another important concept involves the revolution of the earth about the sun, or as seen from the observer, the apparent motion of the sun about the earth. The

mean plane of the earth's orbit around the sun is called the ecliptic plane and is inclined approximately 23.5 deg with respect to the earth's mean equator. The apparent motion of the sun on the celestial sphere as seen from the earth follows the ecliptic plane. The intersection of the earth's equatorial plane with the ecliptic plane creates a line connecting the equinoxes, or line of nodes. The point of intersection where the apparent sun crosses the celestial equator from south to north is termed the first point of Aries, or the vernal equinox.

This framework provides a method for defining the position of objects in space. Using the celestial equator as the fundamental plane and the vernal equinox as a reference point or principal direction, it is possible to define two angular coordinates which uniquely determine the direction of an object with respect to the celestial sphere. Two such angular coordinates are right ascension and declination. Right ascension is the angle measured east from the vernal equinox to the particular hour circle passing through the object being observed. Declination is the angle measured from the celestial equator to the position of the object. [8, 15]

*2.1.2 The Raven Telescope.* The Raven telescope, developed by the Air Force in 1995, is an optical sensor designed to provide high accuracy, deep space observations. Made entirely of commercial-off-the-shelf (COTS) products and fully automated, the .36m Raven performs ballistic tracking with subarcsecond accuracy. The telescope captures images using a charge-coupled device (CCD) with a field of view of 43 x 29 arcseconds. Given this field of view, it is possible to simultaneously track multiple satellites in geosynchronous orbits [12]. CCD images of satellite clusters provide more accurate metrics of vehicle separation since error sources introduced in the observation process are common to each satellite in that frame. Satellite position is then computed using astrometry techniques.

Originally, only one track mode, called sidereal mode, was used. By slewing the telescope at the sidereal rate, stars would appear as points while satellites appeared as streaks. The end points of each streak were then compared with the stellar background



and the time of camera shutter opening or closing was recorded. While this method allowed for accurate fits to the star field, satellite endpoint streak detection introduced a lot of uncertainty. The next mode employed was called stare mode and involved maintaining a stationary telescope position for the duration of the image. In this mode, all of the stars as well as the non-geostationary satellites appeared as streaks, resulting in undesired image clutter. In addition to this issue, stare mode did not alleviate the streak endpoint detection uncertainty. The most recent tracking mode development successfully employed by Raven is termed ballistic or rate track mode. In this mode, the telescope follows the satellite for the duration of the image, producing a point for the satellite and streaks for stars, thus replacing the endpoint detection issue with a centroiding approach [3,12]. A Raven image obtained using this method is shown in Figure 2.2.

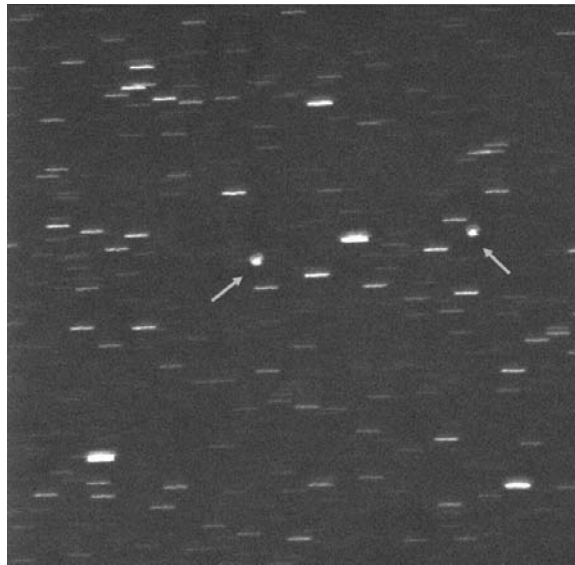


Figure 2.2: Raven Image

*2.1.3 Topocentric to Geocentric Conversion.* When using optical observations it is essential to note the coordinate system in which they are expressed. A geocentric coordinate system has its origin located at the center of the earth while a topocentric coordinate system has its origin translated from the center of the earth to the position of the telescope located on the surface of the earth. In addition to the

translation of origins, the transformation between the two frames involves rotations through the local sidereal time and the compliment of the geodetic latitude. Raven, along with many other earth based optical telescopes, outputs observations expressed in the topocentric frame. Geocentric observations are desirable for the purposes of this research; consequently, it is necessary to perform the appropriate coordinate transformation. The following formulation, shown in Vallado (taken from *Orbital Motion* by Archie E. Roy), determines the geocentric values of right ascension ( $\alpha$ ) and declination ( $d$ ) from the same values in the topocentric frame,  $\alpha_t$  and  $d_t$ , respectively. This formulation also requires the site position magnitude,  $r_{site}$ , and the slant range,  $\rho$ . For the purposes of this research,  $\rho$  will be defined using an average range for a geostationary satellite of 39149 km.

$$\tan \alpha_t - \alpha = \frac{\frac{r_{site}}{\rho} \cos \phi_{gc} \sin \alpha_t - \theta_{LST}}{\cos d_t + \frac{r_{site}}{\rho} \cos \phi_{gc} \cos \alpha_t - \theta_{LST}} \quad (2.1)$$

where  $\phi_{gc}$  is the geocentric latitude, measured positively north from the equator, and  $\theta_{LST}$  is the local mean sidereal time, measured positively to the east from the site. The temporary variable  $\gamma$  is used to complete the formulation:

$$\tan \gamma = \frac{\tan \phi_{gc} \cos \left( \frac{\alpha_t - \alpha}{2} \right)}{\cos \left( \frac{\alpha_t + \alpha}{2} - \theta_{LST} \right)} \quad (2.2)$$

$$\tan d_t - d = \frac{\frac{r_{site}}{\rho} \sin \phi_{gc} \sin d_t - \gamma}{\sin \gamma + \frac{r_{site}}{\rho} \sin \phi_{gc} \cos d_t - \gamma} \quad (2.3)$$

For a more rigorous derivation of the above equations, see Roy(1988,64-67) [15].

## 2.2 *Least Squares Estimation*

The motion of an orbiting body about the Earth is modeled using equations of motion, the most basic of which is the two-body equation. This equation describes an orbit using six orbital elements. Hence, when determining the path of an orbiting body using optical measurements of right ascension and declination, it is necessary to obtain at least three measurements - six known values result in six solvable values.

Typically however, more than three observations are obtained, and all are assumed to contain some error. This first became an issue in the early 1800's. In response to a mysterious data arc, later shown by Gauss' methods to be the asteroid Ceres, Gauss developed the theory of probability, leading to the Principle of Maximum Likelihood and the method of Least Squares in its full, non-linear form [17].

### 2.2.1 The Principle of Maximum Likelihood. [17]

Given  $N$  independent measurements  $x_i$  of the value we want to know  $x_0$ , the joint probability is simply the product of the individual Gaussian distributions

$$P(x_1, x_2, \dots x_N) = (2\pi)^{\frac{-N}{2}} \left[ \prod_{i=1}^N \sigma_i^{-1} \right] \times \exp \left( - \sum_{i=1}^N \frac{(x_i - x_0)^2}{2\sigma_i^2} \right) \quad (2.4)$$

where  $\sigma_i$  is the standard deviation of each instrument used to obtain measurements. Gauss then proposed that since the true value  $x_0$  is unobtainable, it is reasonable to replace  $x_0$  with an estimate  $\bar{x}$ .

$$P(x_1, x_2, \dots x_N) = (2\pi)^{\frac{-N}{2}} \left[ \prod_{i=1}^N \sigma_i^{-1} \right] \times \exp \left( - \sum_{i=1}^N \frac{(x_i - \bar{x})^2}{2\sigma_i^2} \right) \quad (2.5)$$

Subsequently, the closest value to the truth is found when the estimate maximizes the probability of having gotten the true value. This is shown mathematically when the argument of the exponential in Equation(2.5) is minimized, or its derivative is driven to zero.

$$\frac{d}{d\bar{x}} \sum_{i=1}^N \frac{(x_i - \bar{x})^2}{2\sigma_i^2} = 0 \quad (2.6)$$

Thus the name *the method of least squares*.

### 2.2.2 Linearized Dynamics and the State Transition Matrix. [17]

In most estimation problems, the estimate of multiple values is required. One portion of this thesis, for example, is interested in determining the position and velocity differences between two satellites. These values are typically organized in the form of

a system state vector,  $\mathbf{x}$ . How the state vector changes with time can be expressed using the equations of motion

$$\frac{d\mathbf{x}}{dt} = \mathbf{g}(\mathbf{x}, t) \quad (2.7)$$

or the explicit solution in terms of the initial state and time

$$\mathbf{x}(t) = \mathbf{h}(\mathbf{x}(t_0), t) \quad (2.8)$$

Either of these equations specify how the true state  $\mathbf{x}_0$ , the estimated state  $\bar{\mathbf{x}}$ , and any nearby trajectories change with time.

Assuming that the estimate of the true state is close to the actual state, it is helpful to determine how two close orbits behave with respect to each other. This allows  $\mathbf{x} = \mathbf{x}_0 + \delta\mathbf{x}$  to be substituted into the equations of motion. Equation (2.7) then becomes

$$\frac{d\mathbf{x}}{dt} = \mathbf{g}(\mathbf{x}_0 + \delta\mathbf{x}, t) \quad (2.9)$$

Expanding  $\mathbf{g}$  in a Taylor series about the true trajectory yields

$$\frac{d\mathbf{x}}{dt} \approx \mathbf{g}(\mathbf{x}_0, t) + \nabla_x \mathbf{g}(\mathbf{x}_0, t) \delta\mathbf{x} + O(2) \quad (2.10)$$

leading to the well known Equations of Variation, expressed as

$$\frac{d}{dt} \delta\mathbf{x} = A(t) \delta\mathbf{x} \quad (2.11)$$

where

$$A(t) = \nabla_x \mathbf{g}|_{x_0(t)} \quad (2.12)$$

Because the Equations of Variation are linear ordinary differential equations, a solution can be expressed as the sum of the components  $\delta x_i$  of  $\delta\mathbf{x}$  at  $t_0$  multiplied by

each individual solution vector function  $\vec{\phi}_i$ :

$$\delta \mathbf{x}(t) = \sum_{i=1}^N \delta x_i(t_0) \vec{\phi}_i(t) \quad (2.13)$$

Equation (2.13) can now be simplified by combining the individual components  $\delta x_i$  into the vector  $\delta \mathbf{x}(t_0)$  and the associated individual solutions  $\vec{\phi}_i$  into the matrix  $\Phi$  yielding

$$\delta \mathbf{x}(t) = \Phi(t, t_0) \delta \mathbf{x}(t_0) \quad (2.14)$$

This equation then shows that the state transition matrix  $\Phi$  describes how a change in the initial conditions of the state propagates forward to the value of the state at some time in the future. As stated above, the system dynamics can also be given in the form of an actual solution in terms of the initial state and the time, Equation (2.8). In this case,  $\Phi$  can also be expressed as

$$\Phi(t, t_0) = \nabla_{\mathbf{x}(t_0)} \mathbf{h}(\mathbf{x}(t_0), t) \quad (2.15)$$

### 2.2.3 Linear Least Squares. [17]

When estimating the linear state of a system at the epoch time  $t_0$  it is necessary to first look at the observations  $\mathbf{z}_i(t_i)$  taken at each observation time  $t_i$ . It is assumed that each observation vector  $\mathbf{z}_i$  is independent of all other observation vectors and has an associated instrumental covariance  $Q_i$  measuring the degree of this independence. Assuming also that there is a linear relationship between the system state and the observations at any time  $t_i$ , an observation could be expressed with the following equation, called the observation relation

$$\mathbf{z}_i(t_i) = H_i \mathbf{x}(t_i) + \mathbf{e}_i \quad (2.16)$$

where  $\mathbf{e}_i$  is the true error in the observations. It is then possible to insert the system dynamics into the observation relation

$$\mathbf{z}_i(t_i) = H_i \Phi(t_i, t_0) \mathbf{x}(t_0) + \mathbf{e}_i \quad (2.17)$$

Simplifying further,

$$\mathbf{z}_i(t_i) = T_i \mathbf{x}(t_0) + \mathbf{e}_i \quad (2.18)$$

where  $T_i \equiv H_i \Phi(t_i, t_0)$ .

It is then common to assemble all vectors and matrices for the N measurements into larger matrices.

$$\begin{aligned} \mathbf{z} &\equiv \begin{pmatrix} \mathbf{z}_1 \\ \mathbf{z}_2 \\ \vdots \\ \mathbf{z}_N \end{pmatrix} \\ T &\equiv \begin{pmatrix} T_1 \\ T_2 \\ \vdots \\ T_N \end{pmatrix} \\ Q &\equiv \begin{pmatrix} Q_1 & 0 & \cdots & 0 \\ 0 & Q_2 & \cdots & 0 \\ \vdots & \vdots & \ddots & \vdots \\ 0 & 0 & \cdots & Q_N \end{pmatrix} \end{aligned} \quad (2.19)$$

Using the method followed in Wiesel [17], the estimate of the state vector at the epoch time  $\bar{\mathbf{x}}(t_0)$  can be stated as follows

$$\bar{\mathbf{x}}(t_0) = (T^T Q^{-1} T)^{-1} T^T Q^{-1} \mathbf{z} \quad (2.20)$$

with the measure of accuracy coming from the covariance matrix expressed as

$$P_{\bar{\mathbf{x}}}(t_0) = (T^T Q^{-1} T)^{-1} \quad (2.21)$$

#### 2.2.4 Nonlinear Least Squares. [17]

Most problems in the real world are in actuality nonlinear problems, either in their dynamics, their observation relations, or both. Linear systems for these problems are typically developed by making certain assumptions. While the linear system of equations may be sufficient for some applications, a more rigorous analysis is often required prompting the usage of nonlinear dynamics and nonlinear observation geometry.

An explicit solution for the system dynamics can be represented as

$$\mathbf{x}(t) = h(\mathbf{x}(t_0), t) \quad (2.22)$$

As Wiesel explains, assuming the dynamics are deterministic, it should follow that their linearization about a reference trajectory  $\mathbf{x}_{ref}$

$$\delta \mathbf{x}(t) = \Phi(t, t_0) \delta \mathbf{x}(t_0) \quad (2.23)$$

is valid, where  $\delta \mathbf{x}$  is the desired change in the reference trajectory that will make the reference trajectory equal to the true trajectory. Since the true trajectory  $\mathbf{x}_0$  is unobtainable,  $\delta \mathbf{x}$  actually corrects the reference trajectory into the closest possible estimate of the true trajectory. Also, the state transition matrix  $\Phi$ , is defined as the gradient of the solution with respect to the initial conditions

$$\Phi(t, t_0) = \nabla_{\mathbf{x}_{t_0}} h(\mathbf{x}(t_0), t) \quad (2.24)$$

The observation relation, a function that will predict the observations given the state vector, can be expressed as

$$\mathbf{z}_i(t_i) = \mathbf{G}(\mathbf{x}(t_i), t_i) \quad (2.25)$$

where  $\mathbf{z}_i(t_i)$  are the measurements taken at different observation times  $t_i$ .

In any measurement a certain amount of error will be present. The value  $\mathbf{z}_0$  is the vector containing perfect measurements which would give the true state  $\mathbf{x}_0$  and  $\mathbf{z}$  is the vector of actual measurements which would give the imperfect observed state  $\mathbf{x}$ . Assuming that the true error in the data goes to zero as the true error in the state goes to zero, the true error in the actual data can be represented as

$$\begin{aligned}\mathbf{e} &= \mathbf{z} - \mathbf{z}_0 = \mathbf{G}(\mathbf{x}, t) - \mathbf{G}(\mathbf{x}_0, t) \\ &= \mathbf{G}(\mathbf{x}_0 + \delta\mathbf{x}, t) - \mathbf{G}(\mathbf{x}_0, t) \\ &\approx \frac{\partial \mathbf{G}}{\partial \mathbf{x}} \delta\mathbf{x}(t)\end{aligned}\tag{2.26}$$

where  $\mathbf{x} = \mathbf{x}_0 + \delta\mathbf{x}$  and the last line in this set of equations relates the error in the state to the error in the reference trajectory. Since it is assumed that the residual  $\mathbf{r}$  will approximate the true error  $\mathbf{e}$ , the equation for the residual becomes

$$\mathbf{r}_i = \mathbf{z}_i - \mathbf{G}(\mathbf{x}_{ref}(t_i), t_i)\tag{2.27}$$

$H$  is then defined as

$$H_i = \frac{\partial \mathbf{G}}{\partial \mathbf{x}}(\mathbf{x}_{ref}(t_i), t_i)\tag{2.28}$$

Using the same form as the last line in Equation (2.26), recognizing that the residual is linearly related to  $\delta\mathbf{x}$ , and recalling Equation (2.23), the equation for the residual then becomes

$$\begin{aligned}\mathbf{r}_i &\approx H_i \delta\mathbf{x}(t_i) = H_i \Phi(t_i, t_0) \delta\mathbf{x}(t_0) \\ &= T_i \delta\mathbf{x}(t_0)\end{aligned}\tag{2.29}$$

The final results, being in the same form as the linear least squares case, can then be written as

$$\delta\mathbf{x}(t_0) = (T^T Q^{-1} T)^{-1} T^T Q^{-1} \mathbf{r}\tag{2.30}$$



$$P_{\delta\mathbf{x}} = (T^T Q^{-1} T)^{-1} \quad (2.31)$$

and the final estimate of the trajectory is then

$$\bar{\mathbf{x}}(t_0) = \mathbf{x}_{ref}(t_0) + \delta\mathbf{x}(t_0) \quad (2.32)$$

### 2.3 *Relative Motion*

Relative motion describes the position of one satellite with respect to another. With more satellites placed in the GEO belt, relative motion has become an increasingly important tool for analysis of orbit determination and satellite position.

*2.3.1 Equations of Motion.* Relative equations of motion were developed in 1878 when Hill derived a set of equations to describe the moon's orbit around the earth. These equations were then modified by Clohessy and Wiltshire in 1960 to describe relative motion in rendezvous operations. With the aid of several assumptions, these equations are developed based on position and velocity differences between two objects and can be solved analytically. The assumptions associated with this formulation are as follows

1. The reference orbit is circular
2. Earth is spherically symmetric
3. The distance between objects is close when compared to their orbital radii

Due to the limiting assumptions associated with Hill's equations, many other sets of equations have been developed. One such set is known as the Cluster Orbits With Perturbations Of Keplerian Elements (COWPOKE) equations. Using mean Keplerian elements and element differences, a method of expressing the relative equations of motion for objects in non-circular orbits has been developed [13].

#### *2.3.2 Differential Orbital Element Effects.* [10]

When considering relative motion between two or more satellites, an understand-

ing of the effects of differential orbital elements is helpful. The first consideration in maintaining a formation of satellites is the semimajor axis  $a$ . Orbits with different semimajor axes have different periods, resulting in rapid formation dispersion. Avoiding this dispersion requires that the mean semimajor axis for each satellite be the same. Next, inclination  $i$  differences result in out-of-plane separation at higher latitudes. Because each orbit then passes over different portions of the earth, the effects of  $J_2$  on each orbit will be slightly different as well, resulting in differences in nodal precession rates. These differences cause orbital plane separation resulting in increased formation separation. Differences in right ascension of the ascending node  $\Omega$  result in maximum satellite separation at the equator. Coplanar satellites achieve along-track separation by differences in mean anomaly  $M$ , while satellites in eccentric orbits can achieve radial separation by differences in the argument of perigee  $\omega$ .

## ***2.4 Relative Motion Applications in GEO***

As organizations become aware of the slot allocation problem in GEO, more research is being done on existing satellite clusters and unintentional close approach encounters. This section will touch on a few such research efforts.

*2.4.1 GEO Clusters.* As technology develops and demand increases, available slots in the geosynchronous belt become more limited in number. Organizations involved in communications who own one of the coveted slots look for ways to best utilize and exploit the limited space they own. Consequently, more organizations choose to collocate multiple satellites along the same longitude. EUTELSAT is one such organization [9]. To ensure consistent radio and television broadcasting and increase multi-mission capabilities, EUTELSAT has concentrated five satellites on 15 deg East. Given the system requirements, those associated with the orbit control strategy provided the driving constraints. Two categories of constraints were identified. The first constraint, dealing with constraints due to the quality of RF service provided, was easily simplified by coordinating the frequency plans of the satellites

within the cluster. The second, and driving, constraint dealt with those associated with orbit control.

*2.4.1.1 Orbit Control and Stationkeeping Strategies.* Several orbit control and formationkeeping strategies have been presented [3,9]. In deciding on which strategy to employ, each organization must consider the constraints of their system. As in the EUTELSAT system of vehicles, these constraints may include maintaining control box parameters, propellant consumption, minimizing station keeping maneuvers, avoiding simultaneous maneuvers of satellites within the cluster, and addition or removal of satellites. Many commercial communication satellites require a control box of  $\pm 0.1$  deg in both east/west and north/south directions.

Longitude Separation: This strategy involves separating the satellites by mean longitude. For some applications, this technique is adequate. Sauer proposed this to be the simplest way of collocating two satellites with independent missions. By partitioning a stationkeeping deadband of  $\pm 0.1$  deg into two smaller deadbands, one to two additional satellites can be successfully collocated with an existing satellite with minimal impact on existing stationkeeping operations [14]. Pattinson, on the other hand, finds this technique inadequately susceptible to close approaches for clusters consisting of several satellites with a stationkeeping cycle time of two weeks, as with the EUTELSAT cluster located at 15 deg East [9].

Eccentricity Vector Separation: The eccentricity vector, as shown in Vallado, can be mathematically described as,

$$\vec{e} = \frac{\left(v^2 - \frac{\mu}{r}\right) \vec{r} - (\vec{r} \cdot \vec{v}) \vec{v}}{\mu} \quad (2.33)$$

This vector has a magnitude equal to the orbit eccentricity and always points from the center of the Earth to the orbit perigee [15]. Eccentricity vector separation sets the eccentricity vectors of collocated satellites in different directions while maintaining the same longitude. This strategy produces radial separation over the orbit which may

seem adequate, however, several problems may occur. When the satellites are separated in the radial direction alone obstruction of one satellite by the other is possible, leading to a disruption of mission operations. In addition to this, significant position errors may develop due to orbit determination accuracies and maneuver performance uncertainties which would then lead to unacceptable error ellipsoids.

Combined Eccentricity and Inclination Vector Separation: To deal with the problems created by eccentricity vector only separation, a difference in inclination is commonly added to the satellite cluster. As defined by Pattinson [9], the direction of the inclination vector is determined by projecting the orbit pole onto the earth's equatorial plane. It is possible to orient the vector separation such that any occultations are avoided. This configuration, however, is undesirable since the risk of close approaches is still prevalent when radial separation ceases to exist. Another configuration places the inclination vector perpendicular to the eccentricity vector, allowing for satellite separation in the north/south direction when radial separation does not exist. While occultations are still possible, this configuration is preferred over the previous configuration since close approach constraints are mandated while the probability of occultations is typically small. Given these two configurations, it is then possible to optimize the orientation of the eccentricity and inclination vectors such that the close approach constraint is met while minimizing occultations.

*2.4.2 Close Approaches.* Unintentional close approaches are becoming more frequent as the GEO belt becomes more populated. Slot allocation, as determined by the International Telecommunications Union, is based primarily on separation of operational frequencies while physical proximity is often overlooked. This has placed satellites, operated by different organizations, in slots with overlapping longitude stationkeeping boxes [4]. In addition to slot allocation, there remains the ever present possibility of vehicle failure resulting in uncontrollable drift. In August of 1997, an uncontrolled communications satellite, Telstar 401, came within 12 kilometers of GOES-10, an operational meteorological satellite used by the National Oceanic and

Atmospheric Administration (NOAA) [11]. Since that time, Telstar 401 has had over 100 close approaches with operational satellites, at distances as close as two kilometers [1].

## ***2.5 Chapter Outline***

With this information established it is now possible to continue with the subsequent chapters.

Chapter Three gives the overall methodology for the non-maneuver and maneuver models. Derivation of the observation function is explained, and the state vector and dynamics for each model are discussed. The algorithm involved in each estimation run is also presented.

Chapter Four discusses the simulation and real data sets used in this research. Simulated data was created for one non-maneuver scenario and two maneuver scenarios. In addition to simulated data, two sets of data from actual collocated satellites are evaluated and analyzed.

Chapter Five summarizes the results of this study and offers recommendations for future research.

### III. Methodology

This chapter will discuss the process by which the relative separation between two satellites will be estimated along with a possible maneuver and the maneuver time. A discussion on coordinate transformations from a body-fixed frame to the geocentric inertial frame is followed by the formulation of the observation matrix. Next the system dynamics for both the linear and non-linear models is discussed. Finally the algorithm implemented in the computer model is stated.

#### 3.1 *Coordinate Transformation*

Geocentric inertial right ascension and declination are expressed in the earth centered inertial frame, with unit vector  $\hat{n}_x$  pointing in the direction of the vernal equinox, unit vector  $\hat{n}_z$  going through the North Pole, and unit vector  $\hat{n}_y$  completing the right hand rule. Hill's equations, on the other hand, are formulated using a body fixed frame, with unit vector  $\hat{e}_r$  pointing radially away from the center of the earth, unit vector  $\hat{e}_\theta$  in the along track direction, and unit vector  $\hat{e}_z$  in the cross track direction.

In order to properly formulate the observation function, consisting of differential right ascension and differential declination, the position vectors of each satellite must be expressed in the same frame. The transformation between these two frames consist of rotations involving the right ascension of the ascending node  $\Omega$ , inclination  $i$ , and the argument of latitude  $u$ , defined as the angle measured between the ascending node and the satellite position vector. The rotation matrix  $C$  from the body-fixed frame to the geocentric inertial frame can be written as

$$C = \begin{pmatrix} \cos u & \sin u & 0 \\ -\sin u & \cos u & 0 \\ 0 & 0 & 1 \end{pmatrix} \begin{pmatrix} 1 & 0 & 0 \\ 0 & \cos i & \sin i \\ 0 & -\sin i & \cos i \end{pmatrix} \begin{pmatrix} \cos \Omega & \sin \Omega & 0 \\ -\sin \Omega & \cos \Omega & 0 \\ 0 & 0 & 1 \end{pmatrix} \quad (3.1)$$

Performing the matrix operations gives the following expression for  $C$

$$C = \begin{pmatrix} \cos u \cos \Omega - \sin u \cos i \sin \Omega & \cos u \sin \Omega + \sin u \cos i \cos \Omega & \sin u \sin i \\ -\sin u \cos \Omega - \cos u \cos i \sin \Omega & -\sin u \sin \Omega + \cos u \cos i \cos \Omega & \cos u \sin i \\ \sin i \sin \Omega & -\sin i \cos \Omega & \cos i \end{pmatrix} \quad (3.2)$$

### 3.2 The Observation Function and Its Linearization

In determining the relative separation of two satellites, it is necessary to express the given optical data, right ascension  $\alpha$  and declination  $d$ , as a function of the system state, current time, and observation geometry. This is achieved using the observation function  $\mathbf{G}$ . The following discussion shows the formulation of  $\mathbf{G}$ .

The position vector for satellite one  $\bar{\mathbf{R}}_1$ , originating from the center of the earth and expressed in the geocentric inertial frame is

$$\bar{\mathbf{R}}_1 = R_1 \begin{pmatrix} \cos \alpha_1 \cos d_1 & \sin \alpha_1 \cos d_1 & \sin d_1 \end{pmatrix} \begin{pmatrix} \hat{n}_x \\ \hat{n}_y \\ \hat{n}_z \end{pmatrix} \quad (3.3)$$

where  $\alpha$  is the geocentric right ascension and  $d$  is the geocentric declination. See Figure (3.1). The position vector for satellite one can also be expressed in the body

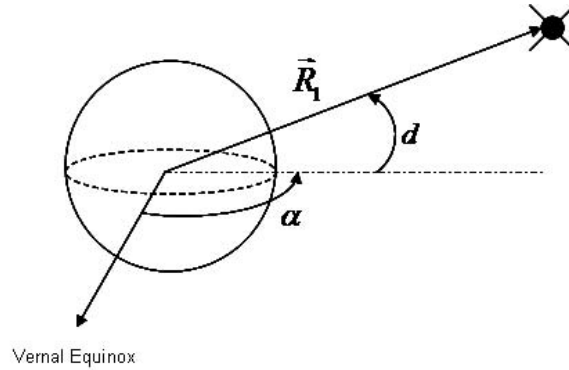


Figure 3.1: Geocentric Inertial Frame

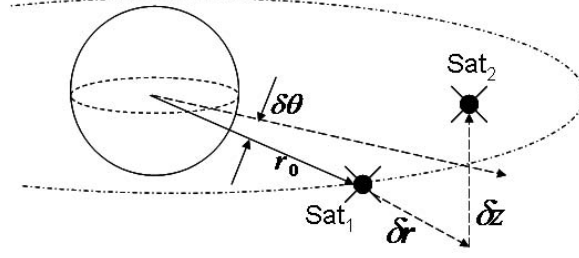


Figure 3.2: Body Fixed Frame

frame as shown in Figure (3.2). Before this vector can be used, however, it must first be rotated to the geocentric inertial frame

$$\bar{\mathbf{R}}_{sat1} = \begin{pmatrix} r_0 & 0 & 0 \end{pmatrix} \begin{pmatrix} \hat{e}_r \\ \hat{e}_\theta \\ \hat{e}_z \end{pmatrix} = \begin{pmatrix} r_0 & 0 & 0 \end{pmatrix} C \begin{pmatrix} \hat{n}_x \\ \hat{n}_y \\ \hat{n}_z \end{pmatrix} \quad (3.4)$$

Setting these two expressions equal to each other yields

$$\begin{aligned} \bar{\mathbf{R}}_1 &= \bar{\mathbf{R}}_{sat1} \\ R_1 \begin{pmatrix} \cos \alpha_1 \cos d_1 \\ \sin \alpha_1 \cos d_1 \\ \sin d_1 \end{pmatrix} &= \begin{pmatrix} r_0 C_{11} \\ r_0 C_{12} \\ r_0 C_{13} \end{pmatrix} \end{aligned} \quad (3.5)$$

Similarly, the expressions for satellite two are

$$\bar{\mathbf{R}}_2 = R_2 \begin{pmatrix} \cos \alpha_2 \cos d_2 & \sin \alpha_2 \cos d_2 & \sin d_2 \end{pmatrix} \begin{pmatrix} \hat{n}_x \\ \hat{n}_y \\ \hat{n}_z \end{pmatrix} \quad (3.6)$$

$$\bar{\mathbf{R}}_{sat2} = \begin{pmatrix} r_0 + \delta r & r_0 \delta \theta & \delta z \end{pmatrix} \begin{pmatrix} \hat{e}_r \\ \hat{e}_\theta \\ \hat{e}_z \end{pmatrix} = \begin{pmatrix} r_0 + \delta r & r_0 \delta \theta & \delta z \end{pmatrix} C \begin{pmatrix} \hat{n}_x \\ \hat{n}_y \\ \hat{n}_z \end{pmatrix} \quad (3.7)$$



$$\bar{\mathbf{R}}_2 = \bar{\mathbf{R}}_{sat2}$$

$$R_2 \begin{pmatrix} \cos \alpha_2 \cos d_2 \\ \sin \alpha_2 \cos d_2 \\ \sin d_2 \end{pmatrix} = \begin{pmatrix} (r_0 + \delta r)C_{11} + r_0\delta\theta C_{21} + \delta z C_{31} \\ (r_0 + \delta r)C_{12} + r_0\delta\theta C_{22} + \delta z C_{32} \\ (r_0 + \delta r)C_{13} + r_0\delta\theta C_{23} + \delta z C_{33} \end{pmatrix} \quad (3.8)$$

The differential position vector, and subsequently the differential right ascension and declination, can then be found by subtracting equations (3.5) and (3.8)

$$\bar{\mathbf{R}}_1 - \bar{\mathbf{R}}_2 = \bar{\mathbf{R}}_{sat1} - \bar{\mathbf{R}}_{sat2} \quad (3.9)$$

producing the following three equations

$$R_2(\cos \alpha_2 \cos d_2) - R_1(\cos \alpha_1 \cos d_1) = (r_0 + \delta r)C_{12} + r_0\delta\theta C_{21} + \delta z C_{31} - R_1 C_{11} \quad (3.10)$$

$$R_2(\sin \alpha_2 \cos d_2) - R_1(\sin \alpha_1 \cos d_1) = (r_0 + \delta r)C_{12} + r_0\delta\theta C_{22} + \delta z C_{32} - R_1 C_{12} \quad (3.11)$$

$$R_2 \sin d_2 - R_1 \sin d_1 = (r_0 + \delta r)C_{13} + r_0\delta\theta C_{23} + \delta z C_{33} - R_1 C_{13} \quad (3.12)$$

Beginning with Equation (3.12), it is possible to obtain an expression for the differential declination,  $\delta d$ . Recalling the following trigonometric formula for some values  $A$  and  $B$

$$\sin A + B = \sin A \cos B + \cos A \sin B \quad (3.13)$$

and setting  $R_2 = R_1 + \delta R$  and  $d_2 = d_1 + \delta d$ , the left side of Equation (3.12) becomes

$$(R_1 + \delta R)(\sin d_1 \cos \delta d + \sin \delta d \cos d_1) - R_1 \sin d_1 \quad (3.14)$$

Substituting this in for the left side of Equation (3.12) and using the small angle assumption, the following equation results

$$R_1 \sin d_1 + \sin d_1 \delta R + R_1 \cos d_1 \delta d - R_1 \sin d_1 = R_1 C_{13} + \delta R C_{13} + R_1 \delta \theta C_{23} + \delta z C_{33} - R_1 C_{13} \quad (3.15)$$

where  $R_1 = r_0$  and  $\delta R = \delta r$ . Simplifying this equation yields

$$\cos d_1 \delta d = -\sin d_1 \frac{\delta R}{R_1} + \frac{\delta R}{R_1} C_{13} + \delta \theta C_{23} + \frac{\delta z}{R_1} C_{33} \quad (3.16)$$

But, recalling Equation (3.5),  $\sin d_1 = C_{13}$  so the  $\delta R$  terms cancel out. Consequently, the following expression for  $\delta d$  results

$$\delta d = \frac{\cos u \sin i}{\cos d_1} \delta \theta + \frac{\cos i}{\cos d_1 R_1} \delta z \quad (3.17)$$

Applying the same method, an expression for differential right ascension,  $\delta \alpha$ , can then be solved for using Equations (3.10) and (3.11).

$$\begin{aligned} \cos \alpha_1 \cos d_1 \delta R - R_1 \sin \alpha_1 \cos d_1 \delta \alpha - R_1 \cos \alpha_1 \sin d_1 \delta d = \\ R_1 C_{11} + \delta R C_{11} + R_1 \delta \theta C_{21} + \delta z C_{31} - R_1 C_{11} \end{aligned} \quad (3.18)$$

$$\begin{aligned} \sin \alpha_1 \cos d_1 \delta R + R_1 \cos \alpha_1 \cos d_1 \delta \alpha - R_1 \sin \alpha_1 \sin d_1 \delta d = \\ R_1 C_{12} + \delta R C_{12} + R_1 \delta \theta C_{22} + \delta z C_{32} - R_1 C_{12} \end{aligned} \quad (3.19)$$

Multiplying Equation (3.18) by  $\sin \alpha_1$ , Equation (3.19) by  $\cos \alpha_1$ , and subtracting Equation (3.18) from (3.19) yields

$$\begin{aligned} R_1 \cos d_1 \delta \alpha_1 = \\ (C_{12} \cos \alpha_1 - C_{11} \sin \alpha_1) \delta R + (C_{22} \cos \alpha_1 - C_{21} \sin \alpha_1) R_1 \delta \theta + \\ (C_{32} \cos \alpha_1 - C_{31} \sin \alpha_1) \delta z \end{aligned} \quad (3.20)$$

Recalling again Equation (3.5),

$$\begin{aligned}\cos \alpha_1 \cos d_1 &= C_{11} \\ \sin \alpha_1 \cos d_1 &= C_{12}\end{aligned}$$

and noting these expressions in the  $\delta R$  term of Equation (3.20)

$$C_{12} \cos \alpha_1 - C_{11} \sin \alpha_1 = 0 \quad (3.21)$$

The expression for differential right ascension then becomes

$$\delta \alpha = \frac{1}{\cos d_1} \left( (C_{22} \cos \alpha_1 - C_{21} \sin \alpha_1) \delta \theta + (C_{32} \cos \alpha_1 - C_{31} \sin \alpha_1) \frac{\delta z}{R_1} \right) \quad (3.22)$$

This expression can be further reduced by recognizing again from Equation (3.5)

$$\begin{aligned}\cos \alpha_1 &= \frac{C_{11}}{\cos d_1} \\ \sin \alpha_1 &= \frac{C_{12}}{\cos d_1}\end{aligned}$$

Considering the  $\delta \theta$  component of equation (3.20)

$$C_{22} \cos \alpha_1 - C_{21} \sin \alpha_1 = \frac{C_{22}C_{11} - C_{21}C_{12}}{\cos d_1} = \frac{\cos i}{\cos d_1} \quad (3.23)$$

Similarly, considering the  $z$  component of Equation (3.20)

$$C_{32} \cos \alpha_1 - C_{31} \sin \alpha_1 = \frac{C_{32}C_{11} - C_{31}C_{12}}{\cos d_1} = -\frac{\sin i \cos u}{\cos d_1 R_1} \quad (3.24)$$

Finally, the expression for differential right ascension becomes

$$\delta \alpha = \frac{1}{\cos^2 d_1} \left( \cos(i) \delta \theta - \frac{\sin i \cos u}{R_1} \delta z \right) \quad (3.25)$$

Having solved for  $\delta d$  and  $\delta \alpha$ , the observation relation  $\mathbf{G}$  is now written as

$$\mathbf{G} = \begin{pmatrix} \delta \alpha \\ \delta d \end{pmatrix} = \begin{pmatrix} \frac{1}{\cos^2 d_1} \left( \cos(i) \delta \theta - \frac{\sin i \cos u}{R_1} \delta z \right) \\ \frac{\cos u \sin i}{\cos d_1} \delta \theta + \frac{\cos i}{\cos d_1 R_1} \delta z \end{pmatrix} \quad (3.26)$$

Due to the linearization about satellite one using Taylor series expansion in the development of  $G$ , its linearization  $H$  is simply

$$H = \frac{\partial \mathbf{G}}{\partial \mathbf{X}} = \begin{pmatrix} 0 & \frac{\cos i}{R_1 \cos^2 d_1} & \frac{\sin i \cos u}{R_1 \cos^2 d_1} & 0 & 0 & 0 \\ 0 & \frac{\cos u \sin i}{R_1 \cos d_1} & \frac{\cos i}{R_1 \cos d_1} & 0 & 0 & 0 \end{pmatrix} \quad (3.27)$$

where the state vector is defined as

$$\mathbf{X} = \begin{pmatrix} \delta r & r_0 \delta \theta & \delta z & \delta \dot{r} & r_0 \delta \dot{\theta} & \delta \dot{z} \end{pmatrix}^T \quad (3.28)$$

### 3.3 Linear System Dynamics

The relative motion between two co-located satellites in geostationary orbit can be described using Hill's equations. Assuming a circular reference orbit and a small distance between satellites, Hill's equations take the following form:

$$\begin{aligned} \delta \ddot{r} - 2nr_0 \delta \dot{\theta} - 3n^2 \delta r &= 0 \\ r_0 \delta \ddot{\theta} + 2n \delta \dot{r} &= 0 \\ \delta \ddot{z} + n^2 \delta z &= 0 \end{aligned} \quad (3.29)$$

As Wiesel [16] explains, these equations can be solved analytically

$$\begin{aligned}
\delta r(t) &= -\left(\frac{2}{n}r_0\delta\dot{\theta}_0 + 3\delta r_0\right)\cos nt + \frac{\delta\dot{r}_0}{n}\sin nt + 4\delta r_0 + \frac{2}{n}r_0\delta\dot{\theta}_0 \\
\delta\theta(t) &= \delta\theta_0 - \left(3\delta\dot{\theta}_0 + \frac{6n\delta r_0}{r_0}\right)t + \left(\frac{4\delta\dot{\theta}_0}{n} + \frac{6\delta r_0}{r_0}\right)\sin nt + \frac{2\delta\dot{r}_0}{nr_0}\cos nt - \frac{2}{nr_0}\delta\dot{r}_0 \\
\delta z(t) &= \delta z_0\cos nt + \frac{\delta\dot{z}_0}{n}\sin nt \\
\delta\dot{r}(t) &= \left(2r_0\delta\dot{\theta}_0 + 3n\delta r_0\right)\sin nt + \delta\dot{r}_0\cos nt \\
\delta\dot{\theta}(t) &= \left(-3\delta\dot{\theta}_0 - \frac{6n\delta r_0}{r_0}\right) + \left(\frac{6n\delta r_0}{r_0} + 4\delta\dot{\theta}_0\right)\cos nt - \frac{2\delta\dot{r}_0}{r_0}\sin nt \\
\delta\dot{z}(t) &= -\delta z_0n\sin nt + \delta\dot{z}_0\cos nt
\end{aligned} \tag{3.30}$$

The solution can then be put into matrix form, represented by the  $6 \times 6$  matrix  $\Phi_{Hill}$ .

$$\Phi_{Hill} = \begin{pmatrix} \Phi_{rr} & \Phi_{rv} \\ \Phi_{vr} & \Phi_{vv} \end{pmatrix} \tag{3.31}$$

The solution for each position component  $(\delta r, r_0\delta\theta, \delta z)$  is found by propagating the initial position components  $(\delta r_0, r_0\delta\theta_0, \delta z_0)$  forward using the  $3 \times 3$  matrix  $\Phi_{rr}$  and the initial velocity components  $(\delta\dot{r}_0, r_0\delta\dot{\theta}_0, \delta\dot{z}_0)$  forward using  $\Phi_{rv}$ . Similarly, the solution for each velocity component  $(\delta\dot{r}, r_0\delta\dot{\theta}, \delta\dot{z})$  is found by propagating the initial position components forward using  $\Phi_{vr}$  and the initial velocity components forward using  $\Phi_{vv}$ . This can be shown in the following equations

$$\delta\mathbf{r} = \Phi_{rr}\delta r(t=0) + \Phi_{rv}\delta v(t=0) \tag{3.32}$$

$$\delta\mathbf{v} = \Phi_{vr}\delta r(t=0) + \Phi_{vv}\delta v(t=0) \tag{3.33}$$

Referring back to Equation (3.31), the full state transition matrix is written as

$$\Phi_{Hill} = \begin{pmatrix} 4 - 3\cos\psi & 0 & 0 & \frac{1}{n}\sin\psi & \frac{2}{n}(1 - \cos\psi) & 0 \\ 6(\sin\psi - \psi) & 1 & 0 & \frac{2}{n}(\cos\psi - 1) & \frac{4}{n}\sin\psi - \frac{3}{n}\psi & 0 \\ 0 & 0 & \cos\psi & 0 & 0 & \frac{1}{n}\sin\psi \\ 3n\sin\psi & 0 & 0 & \cos\psi & 2\sin\psi & 0 \\ 6n(\cos\psi - 1) & 0 & 0 & -2\sin\psi & -3 + 4\cos\psi & 0 \\ 0 & 0 & -n\sin\psi & 0 & 0 & \cos\psi \end{pmatrix} \quad (3.34)$$

where  $n$  is the mean motion of the reference satellite and  $\psi = nt$ . The state vector for the linear model is defined as

$$\mathbf{X} = \begin{pmatrix} \delta r & r_0\delta\theta & \delta z & \delta\dot{r} & r_0\delta\dot{\theta} & \delta\dot{z} \end{pmatrix}^T \quad (3.35)$$

### 3.4 The Maneuver Model: Non-linear System Dynamics

If  $\mathbf{X}_0$  is the initial state of the system, as defined in Equation (3.35), the state of the system at any time  $t$  prior to a maneuver  $\mathbf{X}_{pre}$  can be determined using the state transition matrix given in Equation (3.34)

$$\mathbf{X}_{pre} = \Phi_{Hill}(t, t_0)\mathbf{X}_0 \quad (3.36)$$

The state immediately after a maneuver  $\mathbf{X}_{post}$  can then be defined as the initial state propagated forward to the time of the maneuver  $t_m$  plus the change in state caused by the maneuver  $\Delta\mathbf{X}$

$$\mathbf{X}_{post} = \Phi_{Hill}(t_m, t_0)\mathbf{X}_0 + \Delta\mathbf{X} \quad (3.37)$$

Note that because the satellite will not be instantaneously displaced,  $\Delta\mathbf{X}$  will only consist of velocity components. Using this equation, the state of the system  $\mathbf{X}$  at

some time  $t$  after the maneuver can be written as

$$\begin{aligned}\mathbf{X} &= \Phi_{Hill}(t, t_m)\mathbf{X}_{post} \\ &= \Phi_{Hill}(t, t_m)\Phi_{Hill}(t_m, t_0)\mathbf{X}_0 + \Phi_{Hill}(t, t_m)\Delta\mathbf{X}\end{aligned}\quad (3.38)$$

Simplifying,  $\mathbf{X}$  becomes

$$\mathbf{X} = \Phi_{Hill}(t, t_0)\mathbf{X}_0 + \Phi_{Hill}(t, t_m)\Delta\mathbf{X}\quad (3.39)$$

This can be expressed graphically as shown in Figure 3.3

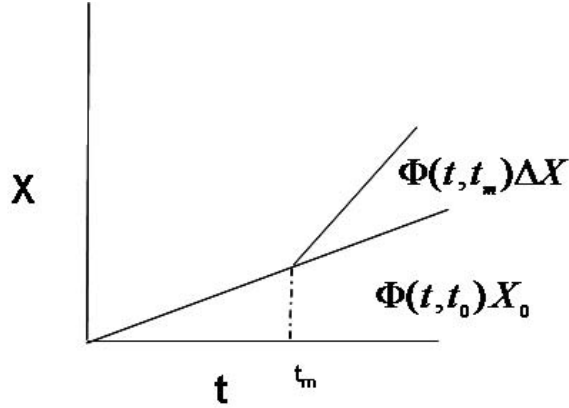


Figure 3.3: Maneuver Dynamics

Because the goal of this research is to estimate the size and direction of the maneuver as well as the maneuver time, the state vector in the non-linear maneuver model will include the  $\Delta\mathbf{X}$  components as well as the change in maneuver time.

$$\mathbf{X}_m = (\delta r, r_0\delta\theta, \delta z, \delta\dot{r}, r_0\delta\dot{\theta}, \delta\dot{z}, \Delta v_r, \Delta v_\theta, \Delta v_z, \delta t_m)^T\quad (3.40)$$

where  $\Delta v_r$ ,  $\Delta v_\theta$ , and  $\Delta v_z$  are the changes in velocity in the  $\delta r$ ,  $r_0\delta\theta$ , and  $\delta z$  directions respectively, and  $\delta t_m$  is the change in the estimate of the maneuver time.

The state transition matrix  $\Phi_{maneuver}$  then becomes a  $10 \times 10$  matrix with the upper  $6 \times 6$  being the solution to Hill's equations,  $\Phi_{Hill}$ , as seen in Equation (3.34).

The next  $6 \times 3$  portion of  $\Phi_{maneuver}$  propagates  $\Delta \mathbf{X}$  forward in time. This will be done using the  $3 \times 3$  velocity matrices from the solution to Hill's equations,  $\Phi_{rv}$  and  $\Phi_{vv}$  as shown in Equation (3.31). The final  $6 \times 1$  in the upper portion of  $\Phi_{maneuver}$  propagates the estimate for the maneuver time. Recalling Equation (3.39) and Figure 3.3, this column is the partial derivative of  $\Phi_{Hill}(t, t_m)$  with respect to the maneuver time, which is simply the partial derivatives of  $\Phi_{rv}$  and  $\Phi_{vv}$  (replacing the  $\delta \dot{r}$ ,  $r_0 \delta \dot{\theta}$ , and  $\delta \dot{z}$  components with  $\Delta v_r$ ,  $\Delta v_\theta$ , and  $\Delta v_z$ ) with respect to the maneuver time. The equations are shown below

$$\begin{aligned}
\frac{\delta r}{\delta t_m} &= -2r_0 \Delta v_\theta \cos[n(t - t_m)] - \Delta v_r \cos[n(t - t_m)] \\
\frac{r_0 \delta \dot{\theta}}{\delta t_m} &= -4r_0 \Delta v_\theta \cos[n(t - t_m)] + 2\Delta v_r \sin[n(t - t_m)] + 3r_0 \Delta v_\theta \\
\frac{\delta z}{\delta t_m} &= -\Delta v_z \cos[n(t - t_m)] \\
\frac{\delta \dot{r}}{\delta t_m} &= -2r_0 \Delta v_\theta \cos[n(t - t_m)] + \Delta v_r n \sin[n(t - t_m)] \\
\frac{r_0 \delta \dot{\theta}}{\delta t_m} &= 4r_0 \Delta v_\theta n \sin[n(t - t_m)] + 2\Delta v_r n \cos[n(t - t_m)] \\
\frac{\delta \dot{z}}{\delta t_m} &= \Delta v_z n \sin[n(t - t_m)]
\end{aligned} \tag{3.41}$$

The bottom  $4 \times 6$  (rows 7 through 10, columns 1 through 6) are the partial derivatives of the  $\Delta v$  components and the maneuver time with respect to the position and velocity components, which are all zero. The final  $4 \times 4$  (rows 7 through 10, columns 7 through 10) are the partial derivatives of the  $\Delta v$  components and the maneuver time with respect to themselves, giving an identity matrix. The full  $\Phi_{maneuver}$  is shown below.



$$\Phi_{maneuver} = \left( \begin{array}{cc|c} & & \\ & \Phi_{rv} & \frac{\partial \bar{r}}{\partial t_m} \\ & 3 \times 3 & \\ \hline & \Phi_{vv} & \frac{\partial \bar{v}}{\partial t_m} \\ & 3 \times 3 & \\ \hline 0 & & \\ 4 \times 6 & I & 4 \times 4 \end{array} \right) \quad (3.42)$$

### 3.5 Algorithm

This section will outline the algorithm that was used in the estimation program including the type of data used, initialization of the state vector and the reference orbit, and the least squares method.

*3.5.1 Data Files.* As the telescope tracks two satellites, it records a data arc for each vehicle consisting of  $n$  observations of right ascension and declination as well as the time associated with each observation. Because relative equations of motion solve for the separation between two objects, it is necessary to have the right ascension and declination differences,  $\delta\alpha$  and  $\delta d$ , respectively, for each time rather than the absolute right ascension and declination for each satellite. Recalling Section 2.1.3, Raven observations are expressed in the topocentric frame. Before the observations are differenced, it is necessary to convert the observations from the topocentric frame to the geocentric frame as explained in the same section. Once the conversion is completed, the observations are differenced and compiled in an  $n \times 2$  matrix  $\mathbf{z}$ . A standard deviation of approximately 10 arcseconds, or  $4.848 \times 10^{-5}$  radians, is assigned for each component of the relative observations. These values are then compiled in the instrumental covariance matrix  $Q$ , often referred to as the observation weighting

matrix

$$Q = \begin{pmatrix} (4.848 \times 10^{-5})^2 & 0 \\ 0 & (4.848 \times 10^{-5})^2 \end{pmatrix} \quad (3.43)$$

*3.5.2 Initializing the State Vector.* Recalling Equation (3.35), the state vector for the linear non-maneuver model is

$$\mathbf{X} = (\delta r, r_0 \delta \theta, \delta z, \delta \dot{r}, r_0 \delta \dot{\theta}, \delta \dot{z})^T$$

Because the relative separation is assumed to be small, this state is initialized using a zero vector.

Initialization for the non-linear maneuver model is less straight forward. Recalling Equation (3.40), the vector is

$$\mathbf{X}_m = (\delta r, r_0 \delta \theta, \delta z, \delta \dot{r}, r_0 \delta \dot{\theta}, \delta \dot{z}, \Delta v_r, \Delta v_\theta, \Delta v_z, \delta t_m)^T$$

The first six components are still set with an initial value of zero along with  $\delta t_m$ . To initialize the  $\Delta v$  components, it is necessary to recall the partial derivatives of position and velocity with respect to  $\delta t_m$ , as shown in Equation (3.41). It can be seen that every component in these equations is dependent upon one of the  $\Delta v$  components. In order to avoid observability problems, it then follows that at least one of the three  $\Delta v$  components must be non-zero. Referring to the discussion in Section 2.4, most stationkeeping maneuvers in GEO clusters are in the east-west or north-south directions, equating to burns in the along-track,  $r_0 \delta \theta$ , or cross-track,  $\delta z$ , directions. Various values under 2 m/s are then used as initial values in either the  $r_0 \delta \theta$  or  $\delta z$  directions. The maneuver time itself  $t_m$  is perhaps the most difficult parameter to initialize. Without *a priori* information, the entire estimation process must be run for different possible maneuver times. This is done by looping through the time vector, using each observation time as an initial value for the maneuver time.

*3.5.3 Reference Orbit.* The next step in the algorithm involves defining a reference orbit for satellite one. This is done using the NORAD Two-Line Element set (TLE). Six parameters are extracted from the TLE: inclination  $i$ , eccentricity  $e$ , right ascension of the ascending node  $\Omega$ , argument of perigee  $\omega$ , mean anomaly  $M$ , and mean motion  $n_0$ . The semimajor axis  $a$  is solved for using the mean motion; however, the typical two body conversion cannot be used. This is because the mean motion given in the TLE  $n_0$  is actually the "mean" mean motion. The following equations recover  $a$  and  $n$  from the altered  $n_0$  given by the TLE:

$$\begin{aligned}
a_1 &= \left( \frac{k_e}{n_0} \right)^{\frac{3}{2}} \\
\delta_1 &= \frac{3k_2 (3 \cos^2 i_0 - 1)}{2a_1^2 (1 - e_0^2)^{\frac{3}{2}}} \\
a_0 &= a_1 \left( 1 - \frac{1}{3}\delta_1 - \delta_1^2 - \frac{134}{81}\delta_1^3 \right) \\
\delta_0 &= \frac{3k_2 (3 \cos^2 i_0 - 1)}{2a_0^2 (1 - e_0^2)^{\frac{3}{2}}} \\
n &= \frac{n_0}{1 + \delta_0} \\
a &= \frac{a_0}{1 - \delta_0}
\end{aligned} \tag{3.44}$$

where  $k_e = \sqrt{GM_e}$ , with  $G$  defined as the universal gravitational constant and  $M_e$  as the mass of the earth, and  $k_2 = 5.413080 \times 10^{-4}$  [6].

Once the complete set of Classical Orbital Elements (COEs) for the reference orbit and the mean motion have been obtained, it is possible to continue with the algorithm. These values will be used to propagate the reference orbit to each observation time and solve for  $\alpha_1$  and  $d_1$  of satellite one, as described below.

*3.5.4 Least Squares Algorithm.* An observation, consisting of  $\delta\alpha$  and  $\delta d$ , and its associated time is read into the loop.  $\mathbf{X}_0$  is propagated forward from the initial

time to the observation time using Hill's equations expressed in  $\Phi_{Hill}$

$$\mathbf{X} = \Phi_{Hill} \mathbf{X}_0 \quad (3.45)$$

The reference orbit is then propagated forward to the observation time using either two-body dynamics  $M = M_0 + nt_{ob}$  or the SGP4 propagator. The updated COEs are converted to position  $\mathbf{r}$  and velocity  $\mathbf{v}$  vectors, which are then used to solve for the right ascension and declination of satellite one,  $\alpha_1$  and  $d_1$ , respectively.

$$\alpha_1 = \tan^{-1} \left( \frac{r_3}{r_1} \right) \quad (3.46)$$

$$d_1 = \sin^{-1} \left( \frac{r_3}{|\mathbf{r}|} \right) \quad (3.47)$$

These values are then used, along with  $i$  and  $u$  (recalling that  $u$  is defined as the angle measured between the ascending node and the satellite position vector, or  $u = \omega + \nu$  where  $\omega$  is the argument of perigee and  $\nu$  is the true anomaly), to calculate the observation matrix  $\mathbf{G}$  and its linearization  $H$  as defined in Equations (3.26) and (3.27). Once  $\mathbf{G}$  and  $H$  have been obtained the matrix operations of the least squares method, as described in Section 2.2, are performed. These steps are listed briefly below:

1. Solve for  $T$ , recalling  $T_i = H_i \Phi$
2. Calculate the residuals,  $\mathbf{r}_i = \mathbf{z}_i - \mathbf{G}(x)$
3. Add new terms to the sums of the matrix

$$\sum_i T_i^T Q_i^{-1} T_i$$

and the vector

$$\sum_i T_i^T Q_i^{-1} \mathbf{r}_i$$

This process is repeated until each observation has been processed. The remaining steps are listed below.

1. Calculate the covariance matrix  $P_{\delta X}$

$$P_{\delta X} = \left( \sum_i T_i^T Q_i^{-1} T_i \right)^{-1}$$

2. Calculate the state correction vector at the epoch time

$$P_{\delta X} \sum_i T_i^T Q_i^{-1} \mathbf{r}_i$$

3. Calculate the new estimate of the reference trajectory

$$\mathbf{X}_0(t_0) = \mathbf{X}_0(t_0) + \delta \mathbf{X}(t_0)$$

This entire process is then repeated for a set number of iterations or until the system has converged. Once this is accomplished, a new value is used to initialize the maneuver time and the program is repeated.

## IV. Simulations and Real Data

### 4.1 *Relative Orbit Determination Experiment*

In July of 2003, Raven obtained images of the DirecTV 4S and AMC-4 spacecraft collocation at 101 deg West longitude. Observations were taken during the nights of 23 - 24 July and 29 July - 1 August. These observations were then used by researchers at the Air Force Maui Optical and Supercomputing site to determine if the relative separation between two satellites could be more accurately predicted than the absolute position of each vehicle [5]. The relative motion of the satellites was estimated using the COWPOKE equations, and the resulting differences in right ascension and declination were compared to the differences based on the available TLE from 27 July, referred to as TLE2. It was determined that the relative motion did indeed fit the data better than the solution provided by the TLE. One such example is shown in Figure 4.1.

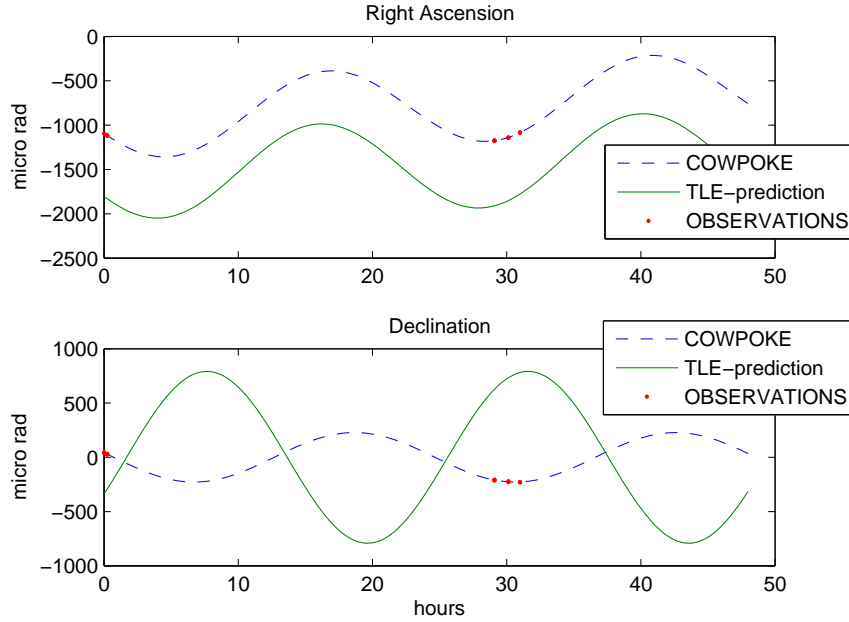


Figure 4.1: COWPOKE and TLE predictions for observations on 30,31 July

During the process of conducting the study, however, it was found that there was an occasional unexplained shift away from the actual position in both the COWPOKE

and TLE predictions. Looking further into the situation, it was determined to be highly likely that stationkeeping maneuvers had taken place; AMC-4, referred to as Sat 1, may have maneuvered sometime between 29 and 30 July, and DirecTV 4S, referred to as Sat 2, may have maneuvered sometime between 31 July and 1 August. Figure 4.2 shows the differences in right ascension and declination, in microradians, between the two satellites. A solution was found using observations from 30 and 31 July and propagated forward through 1 August. As can be seen, the COWPOKE solution fits the data from the 30<sup>th</sup> and 31<sup>st</sup>; however the observations from the 1<sup>st</sup> have shifted away from the predicted values.

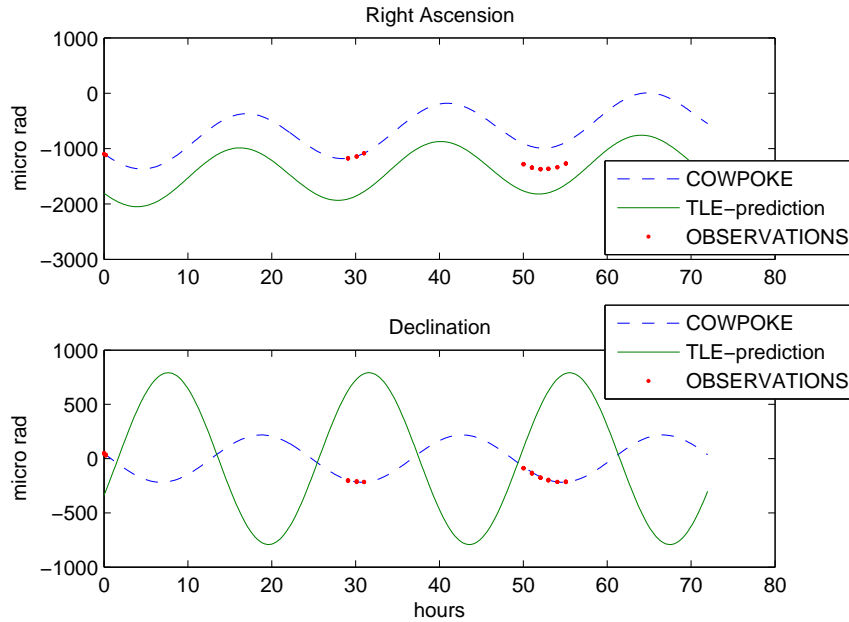


Figure 4.2: Fit to 30<sup>th</sup> and 31<sup>st</sup>, Predict to 1<sup>st</sup>

## 4.2 Simulation Study

*4.2.1 Non-maneuver Model Initial Simulation.* The first simulation created was intended to simply ensure the non-maneuver model was working properly. The reference orbit for Sat 1 was taken from TLE2 while the initial state vector  $\mathbf{X}_0$ , consisting of the position and velocity differences between the satellites, was chosen

to have a separation of 1750m in the along-track or  $r_0\delta\theta$  direction.

$$\mathbf{X}_0 = \begin{pmatrix} 0 & 1750 & 0 & 0 & 0 & 0 \end{pmatrix}^T \quad (4.1)$$

The simulation was then run for one day (86400s) with a step size of 600s. At each time step the reference orbit was propagated forward, and the position and velocity vectors of Sat 1 were computed. Using the method described in Section 3.5.4 and Equations (3.46) and (3.47), the right ascension  $\alpha_1$  and declination  $d_1$  were then calculated for Sat 1. These values, along with  $i$  and  $u$ , were used to calculate the differential right ascension and declination,  $\delta\alpha$  and  $\delta d$ , respectively, using the observation function found in Equation (3.26) and shown again below

$$\mathbf{G} = \begin{pmatrix} \delta\alpha \\ \delta d \end{pmatrix} = \begin{pmatrix} \frac{1}{\cos^2 d_1} \left( \cos(i)\delta\theta - \frac{\sin i \cos u}{R_1} \delta z \right) \\ \frac{\cos u \sin i}{\cos d_1} \delta\theta + \frac{\cos i}{\cos d_1 R_1} \delta z \end{pmatrix} \quad (4.2)$$

The output of the observation function was then compiled in a file and read into the non-maneuver, linear least squares estimation model.

Given the true  $\mathbf{X}_0$  as shown in Equation (4.1) the estimate converged on the correct value with near zero residuals. The root mean square of the residuals ( $r_{rms}$ ) shown below

$$r_{rms} = \frac{\mathbf{r}^T \mathbf{r}}{r} \quad (4.3)$$

was approximately  $4.396 \times 10^{-24}$ . Figure 4.3 shows the trajectory that resulted from the estimated state vector, propagated forward for one day, along with the simulated observations.

*4.2.2 Maneuver Model Initial Simulation.* There are a number of constraints inherent in dealing with operational optical systems. Most telescopes obtain observations only when the sky is dark and the satellites are illuminated by the sun. This effectively limits operations to night time hours. Weather is another factor when dealing with these systems since optical sensors cannot penetrate cloud cover. Due



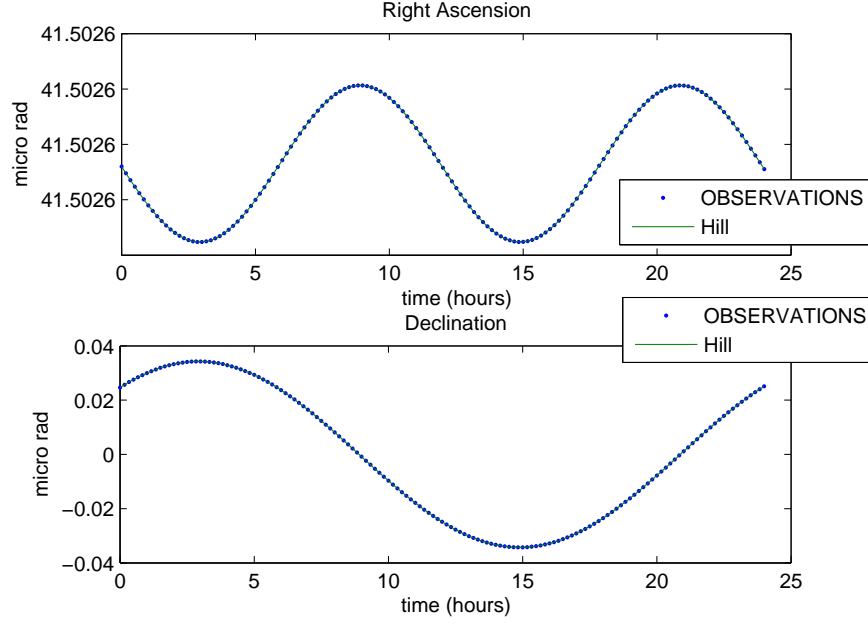


Figure 4.3: Estimated and Simulated Observations

to these constraints, a single telescope is not capable of tracking a satellite or cluster of satellites over a complete revolution. This leads to periods of time (ranging from hours to days) where observations are not available. While satellite motion is deterministic, maneuvers can significantly alter a satellite's orbit, requiring frequent updates to the orbit determination prediction. The gaps between observations could serve to inhibit this process by limiting the amount of necessary information available to accurately determine the current orbit of the satellites.

With this in mind, two maneuver simulations were created. The first simulation used simulated data with perfect observations in similar quantities and times to that found in the real DirecTV 4S and AMC-4 collocation data files. Because two maneuvers were suspected between 29 July and 1 August, this study will focus on those four days. The second simulation used continuous simulated data with perfect observations around the entire orbit for the duration of one day. Both simulations were created with the same initial state vector, as shown here

$$\mathbf{X}_0 = \begin{pmatrix} 0 & 1750 & 0 & 0 & 0 & 0 \end{pmatrix}^T \quad (4.4)$$

Another important situation to explore is the behavior of the maneuver model if a maneuver did not take place. Hence, the final simulation involved evaluating the maneuver model when the non-maneuver simulated data, described in Section 4.2.1, was used.

*4.2.2.1 Simulated Non-Continuous Data.* In order to simulate the actual observations of the Direct TV 4S and AMC-4 satellite collocation, it was necessary to determine the time and length of each data arc in the actual observation files. Table 4.1 gives the approximate time (given in hour and minute of that day) and length (shown in the number of observations) of each arc for the days of interest as well as the time between observations within the arc,  $\Delta t$ .

Table 4.1: Data Arc Time and Length for 29 July - 1 August

<i>July/Aug</i>	<i>Hour</i>	<i>Minute</i>	<i>Obs</i>	$\Delta t$ ( <i>s</i> )
29	7	35-36	5	16
	8	35-36	5	16
	9	32-33	5	16
	10	33-34	5	16
30	6	32-33	4	16
	6	45-46	5	16
31	11	37-38	5	16
	12	39-40	5	16
	13	31-32	5	16
1	8	32-33	5	16
	9	32-33	5	16
	10	34-35	5	16
	11	30-31	5	16
	12	34-35	5	16
	13	35-36	5	16

Three days of simulated data were then created to imitate the data arcs observed in the real data. This was accomplished using the observation function  $\mathbf{G}$  to produce each pair of observations,  $\delta\alpha$  and  $\delta d$ , within the arc. Table 4.2 gives the time and length of each simulated arc as well as the time between observations within the arc.

Table 4.2: Simulated Data Arc Time and Length

<i>Day</i>	<i>Hour</i>	<i>Minute</i>	<i>Obs</i>	$\Delta t$ ( <i>sec</i> )
1	7	35-36	5	16
	8	35-36	5	16
	9	35-36	5	16
	10	35-36	5	16
2	6	35-36	4	16
	6	45-46	5	16
3	11	37-38	5	16
	12	37-38	5	16
	13	37-38	5	16

As in the real data files, the epoch of the estimation run,  $t = 0$ , is the time of the first observation. For instance, the epoch time of this simulation was hour 7, minute 35 on the first day. All times referred to hereafter will be seconds from  $t = 0$  unless otherwise specified as the hour and minute of a particular day.

A change in velocity of 2 m/s was added at  $t = 90000$  s (hour 8, minute 35 on Day 2) to the state  $\mathbf{X}(t = 90000)$  in the along-track or  $r_0\delta\theta$  direction.

$$\mathbf{X}_0 = \mathbf{X}(t = 90000) + \begin{pmatrix} 0 & 0 & 0 & 0 & 2 & 0 \end{pmatrix}^T \quad (4.5)$$

Note that there are no observations within five hours of the maneuver.

In order to determine the range of values for the initial maneuver time guess that will result in convergence on the correct maneuver time, the estimation program was looped through for  $t_m$  equal to each observation time. Once a baseline range was determined, the simulation was run again using a smaller time step for the initial  $t_m$  values. The state vector for each run was initialized using the truth state vector, that used to create the simulated data:

$$\mathbf{X}_0 = \begin{pmatrix} 0 & 1750 & 0 & 0 & 0 & 0 & 0 & 2 & 0 & 0 \end{pmatrix}^T \quad (4.6)$$

Results: An initial guess for the maneuver time within approximately 3.5 hours before 90000 and 2.5 hours after 90000 resulted in alternating convergence on the correct value of  $t_m = 90000$  and the incorrect value of  $t_m = 87138$ . The beginning and end times associated with each span of initial maneuver times, the length of each span, and the resulting maneuver time converged upon are shown in Table 4.3.

Table 4.3: Convergence Times and Values for Simulated Data Arcs

<i>Begin (s)</i>	<i>End (s)</i>	<i>Span (min)</i>	<i>t<sub>m</sub> (s)</i>
74520	74760	4	90000
76200	76980	13	87138
77040	77460	7	90000
77520	80820	55	87138
81660	82560	15	90000
82620	87960	89	87138
88020	91800	63	90000
91860	95400	59	87138
95460	95940	8	90000
96420	98340	32	87138

In addition to the maneuver time, it is beneficial to look at the solution of the state vector. Table 4.4 gives the truth state vector as well as the solution to the state vector for each of the above  $t_m$  convergence values, with the position components given in meters, the velocity components given in meters per second, and the time components given in seconds. Observing the state vector solutions, it becomes obvious that  $t_m = 90000$  produces the correct solution. However, without *a priori* knowledge of the truth state vector, it would be difficult if not impossible to determine which solution is correct.

It is also worth noting the standard deviation,  $1\sigma$ , of the maneuver time for each solution. A maneuver time of 90000 produced a  $1\sigma$  value of 26257 s (approximately 7 hrs and 20 min) while the  $t_m = 87138$  solution produced a  $1\sigma$  value of 27430 s (approximately 7 hrs and 35 min). This essentially says there a lot of uncertainty in these solutions.

Table 4.4: State Vector Solution for Convergence Times

$\mathbf{X}_0$	<i>Truth</i>	$t_m = 90000$	$t_m = 87138$
$\delta r$	0	-3.0642e-010	1220.6
$r_0\delta\theta$	1750	1750	3722.8
$\delta z$	0	-1.0123e-014	-1.1215e-012
$\delta\dot{r}$	0	7.5276e-015	-0.030211
$r_0\delta\dot{\theta}$	0	3.7526e-014	-0.14942
$\delta\dot{z}$	0	-7.0333e-019	-2.788e-015
$\Delta v_r$	0	-8.7235e-014	-0.79629
$\Delta v_\theta$	2	2	1.9714
$\Delta v_z$	0	7.2749e-019	2.9755e-015
$\delta t_m$	0	-1.2407e-009	-2.2473e-009

4.2.2.2 *Simulated Continuous Data.* The next simulation contained continuous simulated data with perfect observations (no noise). This simulation began with the same initial state vector  $\mathbf{X}_0$  as used in the above simulations but spanned one entire day with observations every 600 s (10 min). The orbit was propagated for half of one day (43200 s) and a maneuver of 2 m/s was added at the end of this time period ( $t_m = 43200$  s) in the along-track or  $r_0\delta\theta$  direction.

$$\mathbf{X}_0 = \mathbf{X}(t = 43200) + \begin{pmatrix} 0 & 0 & 0 & 0 & 2 & 0 \end{pmatrix}^T \quad (4.7)$$

The orbit was then propagated for another half day. Differential right ascension and declination values were generated using the observation function  $\mathbf{G}$ .

The truth state vector was used to initialize  $\mathbf{X}_0$  in the estimation process, and the range of values for the initial maneuver time guess that would result in convergence on the correct maneuver time was determined, once again, by looping through the algorithm for  $t_m$  equal to each observation time. Once a baseline range was determined, the simulation was run again using a smaller time step between the initial  $t_m$  values.

Results: For the continuous data simulation, it was found that the estimator converged on the correct value for  $t_m$  if its initial guess was within  $\pm 5$  hours of the

actual time, 43200s. These results produced a  $1\sigma$  value of approximately 11 min with the solution to the state vector shown in Table 4.5.

Table 4.5: State Vector Solution for Convergence Times

$\mathbf{X}_0$	<i>Truth</i>	$t_m = 43200$
$\delta r$	0	-1.996e-012
$r_0\delta\theta$	1750	1750
$\delta z$	0	2.5015e-016
$\delta\dot{r}$	0	1.494e-016
$r_0\delta\dot{\theta}$	0	2.1308e-016
$\delta\dot{z}$	0	-1.7876e-021
$\Delta v_r$	0	5.039e-016
$\Delta v_\theta$	2	2
$\Delta v_z$	0	6.8903e-020
$\delta t_m$	0	6.1894e-013

*4.2.2.3 Simulated Continuous Data - No Maneuver.* The final simulation involved running the non-maneuver data in the maneuver model. As stated in Section 4.2.1, the initial state vector was chosen to have a separation of 1750m in the along-track or  $r_0\delta\theta$  direction.

$$\mathbf{X}_0 = \begin{pmatrix} 0 & 1750 & 0 & 0 & 0 & 0 \end{pmatrix}^T \quad (4.8)$$

The simulation was then run for one day (86400s) with a step size of 600s. No maneuver was included in this simulated data.

The state vector was initialized using the truth position and velocity values, that used to create the simulated data. A  $\Delta v$  of 2 m/s in the along-track or  $r_0\delta\theta$  direction was used to initialize the change in velocity values. The complete initial state vector is shown in Equation (4.9).

$$\mathbf{X}_0 = \begin{pmatrix} 0 & 1750 & 0 & 0 & 0 & 0 & 0 & 2 & 0 & 0 \end{pmatrix}^T \quad (4.9)$$

As in the previous maneuver simulations, the range of values for the initial maneuver time guess was determined by looping through the algorithm for  $t_m$  equal to each observation time.

Results: For the continuous non-maneuver data simulation, it was found that for each initial maneuver time that produced a solution, the maneuver model converged on the correct values for position, velocity, and  $\Delta v$  with residuals on the order of  $1 \times 10^{-20}$ . The model, however, was not able to produce a valid solution for the maneuver time. This can be shown by noting that the state vector component  $\delta t_m$  was unable to converge. This makes sense, since there was no maneuver to begin with. The state vector for one solution is shown in Table 4.6.

Table 4.6: State Vector Solution for No Maneuver Data Set in Maneuver Model

$\mathbf{X}_0$	<i>Truth</i>	$t_m = 43200$
$\delta r$	0	4.9931e-012
$r_0 \delta \theta$	1750	1750
$\delta z$	0	6.8314e-017
$\delta \dot{r}$	0	-1.623e-015
$r_0 \delta \dot{\theta}$	0	-9.9941e-016
$\delta \dot{z}$	0	4.6235e-021
$\Delta v_r$	0	4.4057e-016
$\Delta v_\theta$	0	1.7448e-016
$\Delta v_z$	0	-1.214e-019
$\delta t_m$	0	-95371

### 4.3 Raven Data – 2003

Recalling the relative orbit determination experiment, discussed in Section 4.1, two stationkeeping maneuvers were suspected. With a suspected maneuver for Sat 1 sometime between 29 and 30 July and another for Sat 2 sometime between 31 July and 1 August, the observations were grouped into two sets of data, each consisting of three days of observations. The first set of data contained the observations obtained for 29 – 31 July, while the second set of data contained the observations obtained for 30 July – 1 August.

4.3.1 *Data Set 1: 29 – 31 July.* The first set of data, consisting of observations obtained on 29 – 31 July, was used to examine a possible maneuver performed by Sat 1 between the 29<sup>th</sup> and the 30<sup>th</sup> of July.

Running these observations through the non-maneuver model, Figure 4.4 shows that the linear solution to Hill’s equations do not give an accurate fit. Along with the inexact fit to the declination, note the curvature in the first set of arcs shown in the right ascension plot. The state vector solution  $\mathbf{X}_0$  is shown in Table 4.7.

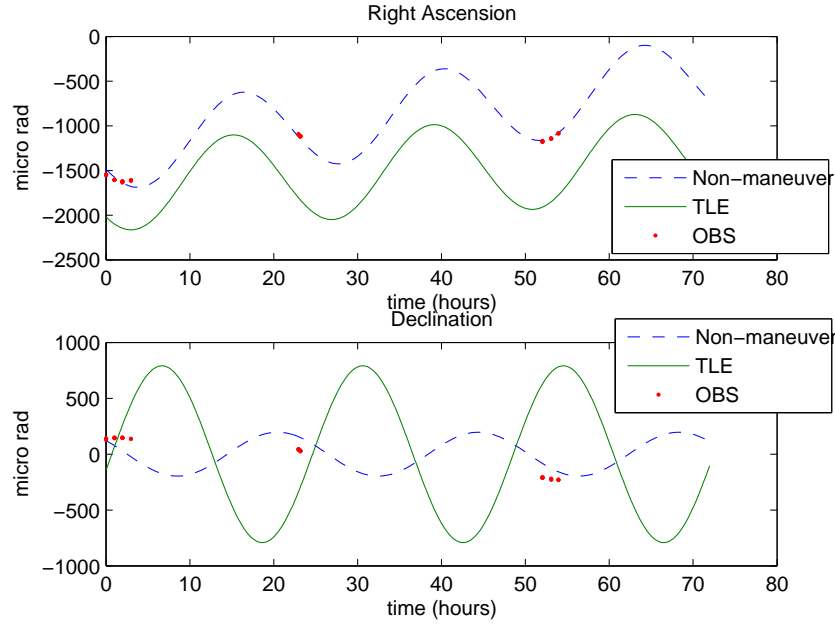


Figure 4.4: Non-maneuver Fit to 29 – 31 July

Table 4.7: State Vector Solution for Non-maneuver Fit to 29 – 31 July

$\mathbf{X}_0$	<i>Solution</i>
$\delta r$	7459.3
$r_0 \delta \theta$	-62665
$\delta z$	5062.6
$\delta \dot{r}$	-0.33898
$r_0 \delta \dot{\theta}$	-1.1306
$\delta \dot{z}$	-0.47661



Valuable insight is also gained by looking at right ascension plotted versus declination, as shown in Figure 4.5. The observations from 29 July can be seen in the

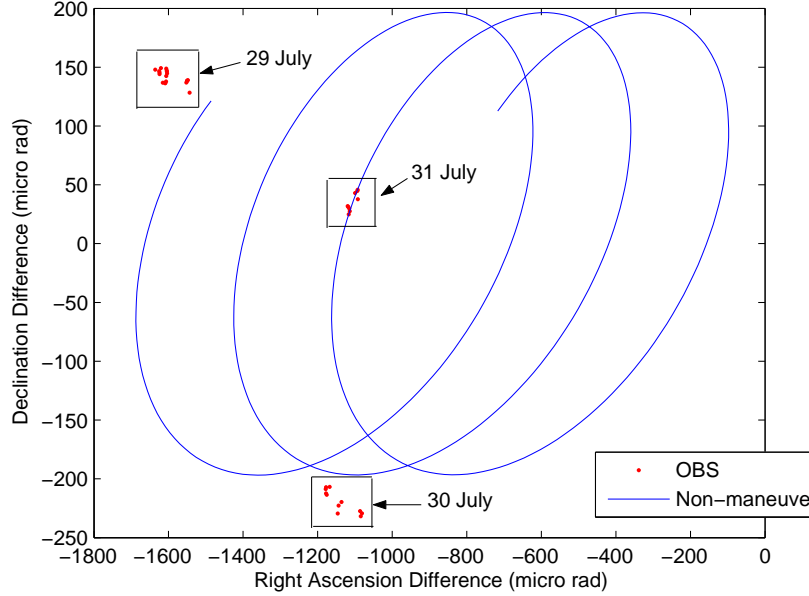


Figure 4.5: Non-maneuver Fit to 29 – 31 July

upper left corner of the plot, located at approximately -1600 microradians on the right ascension axis and 150 microradians on the declination axis (-1600,150). Observations from 30 July are seen at approximately (-1150,-230) and those from 31 July are at (-1050,40). This plot accentuates the inaccuracy of the linear non-maneuver model for this data, noting particularly that the solution does not fit the observations from 29 or 30 July. Along with observing how well the solution fits the data, it is also possible to examine various aspects of the orbital motion. Each ellipse in the solution plot corresponds to the completion of one revolution of the satellites. The shift in these ellipses are due to the secular drift in the along-track direction associated with each orbit. Note that the size, orientation, and drift of each ellipse remains essentially constant.

With the discrepancies in the linear model apparent, the data files are then input into the maneuver model, and the least squares algorithm is run for initial maneuver

time values. These values are obtained by stepping through the time vector at 60 s increments.

Similar to the simulated data presented in Section 4.2.2.1, convergence was achieved upon more than one solution. The first solution was  $t_m = 79477$  which would be during hour 5 on 30 July. This solution was converged upon for initial maneuver time values of approximately 7 hours and 30 min before the assumed maneuver and approximately 2 hours and 7 minutes after the assumed maneuver. The model alternated converging on the final two solutions,  $t_m = 125340$  (hour 18 on 30 July) and  $t_m = 168380$  (hour 6 on 31 July). The times of each convergence is shown in Table 4.8 along with the length of each span, and the solution to the state vector for each maneuver time is shown in Table 4.9.

Table 4.8: Convergence Times and Values for 29-31 July

<i>Begin (s)</i>	<i>End (s)</i>	<i>Span (hr:min)</i>	$t_m$ (s)
52400	87140	9:39	79477
88480	93060	1:16	125340
93180	97260	1:08	168380
115420	120300	1:21	168380
120980	122840	0:31	168380
122960	145240	6:11	125340
152360	182420	8:21	168380

Table 4.9: State Vector Solution for Maneuver Fit to 29 – 31 July

$\mathbf{X}_0$	$t_m = 79477$	$t_m = 125340$	$t_m = 168380$
$\delta r$	5380.3	5410.6	5529.2
$r_0 \delta \theta$	-65297	-65292	-65265
$\delta z$	5673.7	3903	3904.3
$\delta \dot{r}$	-0.67432	-0.67883	-0.69819
$r_0 \delta \dot{\theta}$	-0.84561	-0.84922	-0.86612
$\delta \dot{z}$	0.17538	0.41519	0.41498
$\Delta v_r$	0.30420	-0.2197	0.72159
$\Delta v_\theta$	0.028259	0.094944	-0.21518
$\Delta v_z$	-0.99232	1.1656	-1.1655
$\delta t_m$	-3.3343e-007	-0.00057244	0.00024853

Figure 4.6 shows how the solution for  $t_m = 79477$  fits the data versus time along with the TLE solution and the non-maneuver solution. The maneuver is easily identified in the declination plot at  $t \approx 22$  hrs.

The right ascension versus declination plot, as shown in Figure 4.7, is also evaluated. While this plot confirms that the solution converged upon with the maneuver model fits the data much better than the non-maneuver model, it also reveals a considerable maneuver,  $\Delta v_z \approx -1$  m/s, in the cross-track,  $\delta z$ , or N/S direction. The magnitude and direction of the maneuver, as seen in the solution to the state vector in Table 4.9, could be helpful in analyzing and identifying a particular vehicle.

The solution for  $t_m = 125340$  is shown in Figure 4.8. While the plots for right ascension and declination versus time look reasonable, the right ascension versus declination plot reveals that this solution does not fit the data as well as the solution from  $t_m = 79477$ , particularly in the first set of data arcs. This can be seen in Figure 4.9. Note also the magnitude of the maneuver in this solution:  $\Delta v_z \approx 1.16$  m/s.

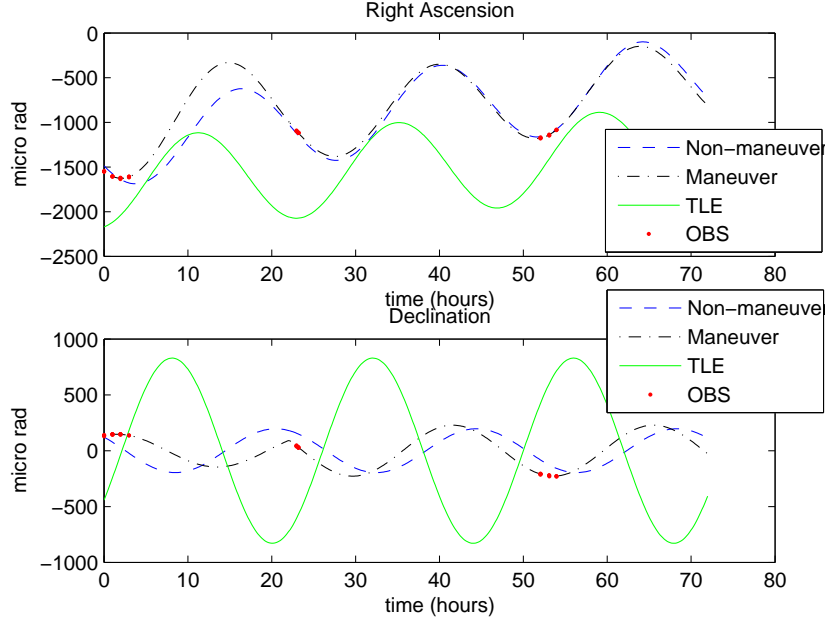


Figure 4.6: Maneuver Fit to 29 – 31 July,  $t_m = 79477$

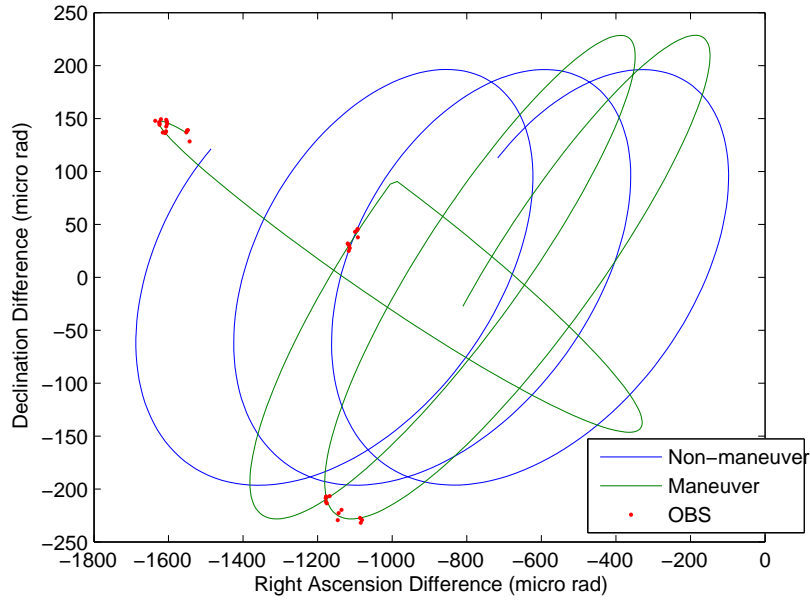


Figure 4.7: RA vs Dec for 29 – 31 July,  $t_m = 79477$

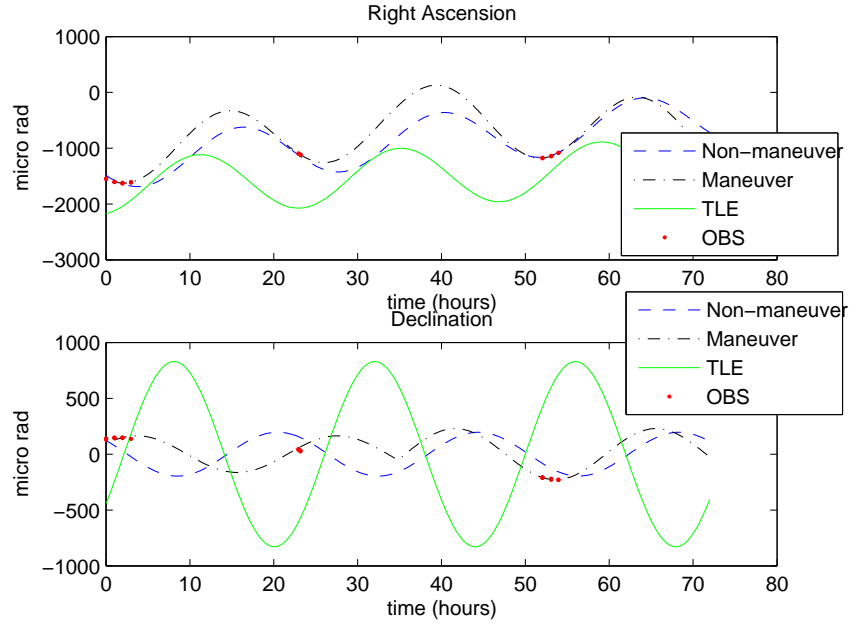


Figure 4.8: Maneuver Fit to 29 – 31 July,  $t_m = 125340$

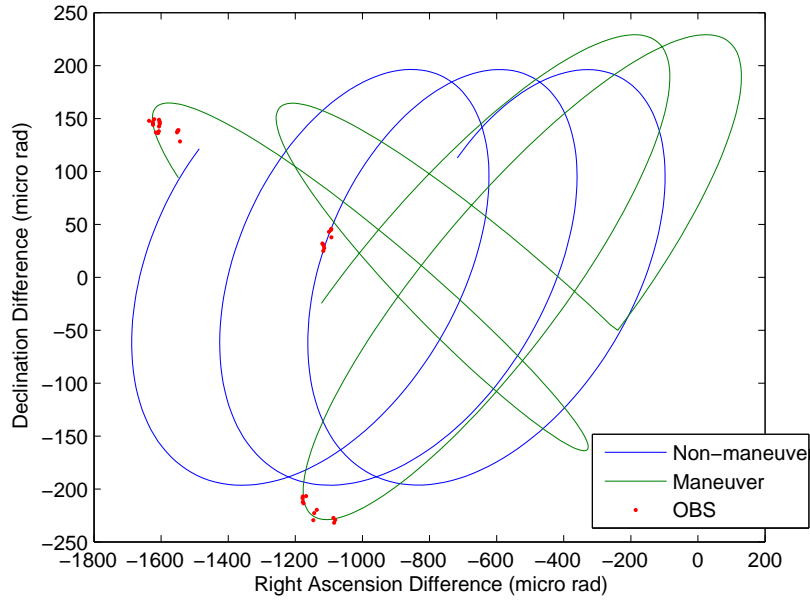


Figure 4.9: RA vs Dec for 29 – 31 July,  $t_m = 125340$

The solution for the final convergence value  $t_m = 168380$  is shown in Figure 4.10. This solution is unlikely due to the growing separation in the right ascension plot. This growth can also be seen in the right ascension versus declination plot shown in Figure 4.11. Note that the solution does not give a good fit for the first set of observations and completely misses the second set of observations. Note also the large magnitude of the maneuver in two directions:  $\Delta v_r \approx 0.72$  and  $\Delta v_z \approx 1.16$  m/s. In many cases, maneuver magnitude can be a useful discrimination tool. If information about a particular collocated satellite is known (such as thruster type, amount of fuel, etc.) it is possible to rule out any solutions that would exceed operational capabilities.

The issue of different solutions for different initial  $t_m$  values, producing apparent local minima, is an important issue to investigate. One possible explanation would be noise inherent in the data. While this could have contributed, the fact that this same phenomenon occurred in the simulated real data (using perfect observations), presented in Section 4.2.2.1, suggests that noise is not the driving factor. Another possible explanation could be that more than one maneuver has taken place. The

plausibility of this situation is validated in another data set as presented in Section 4.4.2. Finally, the most likely explanation lies in the quantity and non-continuous nature of the observations available. As shown by the maneuver simulation results, observability could prove to be the largest obstacle in maneuver estimation. Given the available solutions and analysis in the section above, however,  $t_m = 79477$  was determined to be the most likely solution.

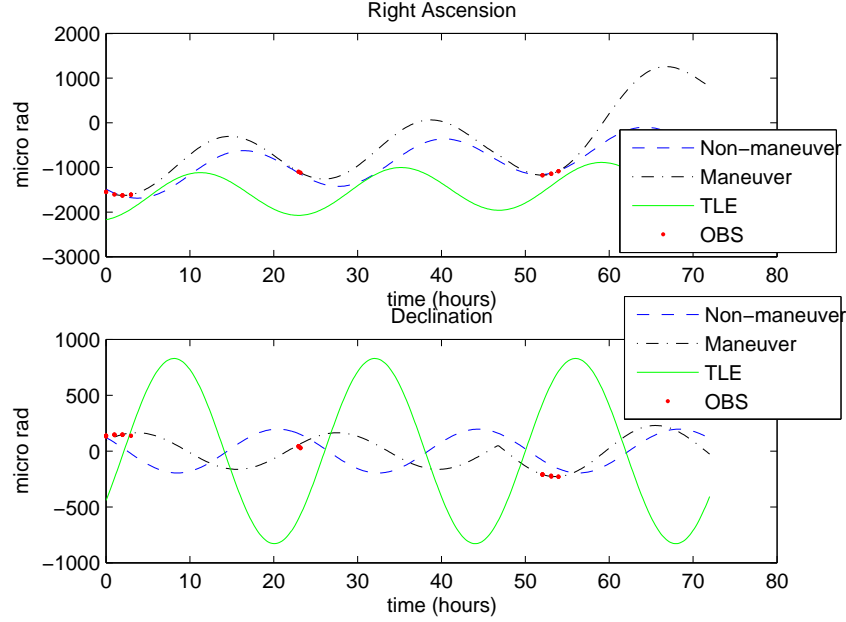


Figure 4.10: Maneuver Fit to 29 – 31 July,  $t_m = 168380$

*4.3.2 Data Set 2: 30 July - 1 August.* The second set of data, consisting of observations obtained on 30 July - 1 August, was used to examine a possible maneuver performed by Sat 2 between the 31<sup>st</sup> of July and the 1<sup>st</sup> of August.

As seen in Figure 4.12, the solution produced by the linear non-maneuver model does not give an accurate fit to these data arcs either. The declination prediction seems to follow the trend in the data; however, the right ascension does not fit the data arcs for 31 July or 1 August. The state vector solution  $\mathbf{X}_0$  is shown in Table 4.10.

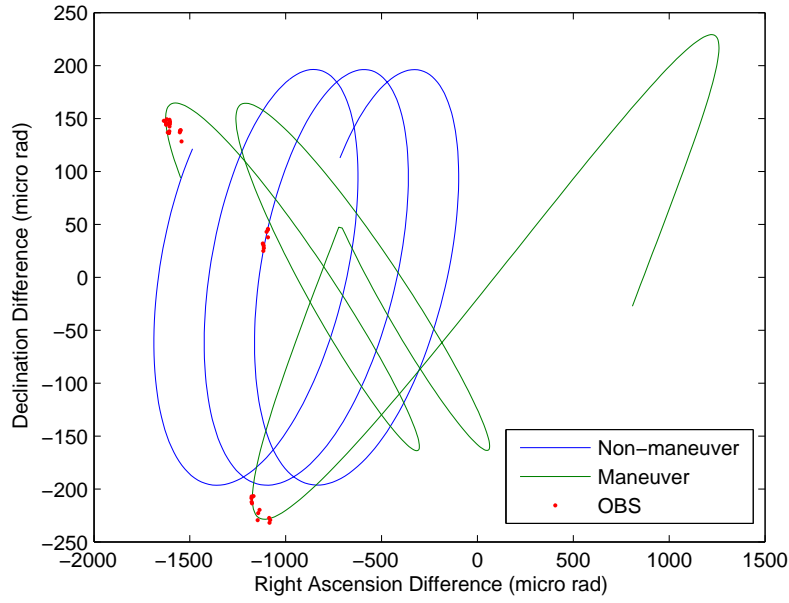


Figure 4.11: RA vs Dec for 29 – 31 July,  $t_m = 168380$

Table 4.10: State Vector Solution for Non-maneuver Fit to 30 July - 1 August

$\mathbf{X}_0$	<i>Solution</i>
$\delta r$	1478.5
$r_0 \delta \theta$	-45779
$\delta z$	1830.2
$\delta \dot{r}$	-0.17368
$r_0 \delta \dot{\theta}$	-0.19512
$\delta \dot{z}$	-0.68939

The data arcs were then run in the maneuver model, and as mentioned above, the least squares algorithm was looped through for each observation time.

While the model produced numerous possible solutions, no convergence was achieved with this data set. Referring back to Table 4.1, the data obtained on 30 July, the first day of this data set, consisted of only nine observations in two arcs separated by 12 minutes. It is therefore most probable that there was not enough data, particularly on the first day, for the estimator to converge upon a solution.

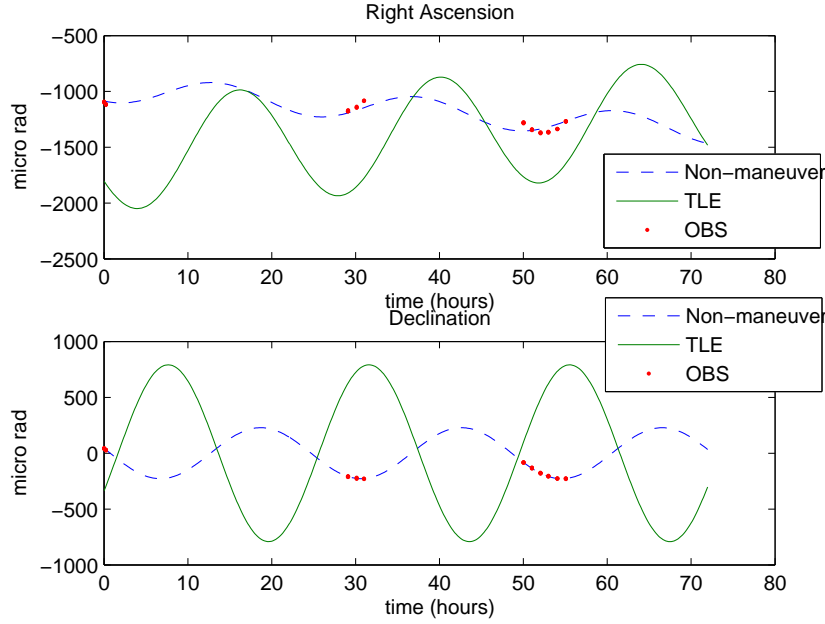


Figure 4.12: Non-maneuver Fit to 31 July - 1 August

#### 4.4 *Raven Data - 2004*

Data for the same collocation was obtained for 3 – 5 and 9 June of 2004. Two maneuvers were suspected; one maneuver was suspected sometime between 3 and 4 June and another sometime between 5 and 9 June. Due to the unobservability between 5 and 9 June, it was decided to focus primarily on the first three days of observations. Similar to the process used for 29 July - 1 August 2003, this data was broken into two different runs. The first data set consisted of 3 and 4 June, with the second data set consisting of observations from 4 and 5 June. These three files have approximately four times the number of observations than those from July 2003. Table 4.11 gives the approximate time (given in hour and minute of that day) and length (shown in the number of observations) of each arc for 3 June as well as the time between observations within the arc,  $\Delta t$ . The data set for 4 June is similar to that of 3 June. It consists of 13 data arcs starting at hour 7 and going through hour 11. There are 10 arcs having 5 observations each and three arcs having 4 observations. Only two arcs were obtained for hour 9, however, one at the beginning of the hour



Table 4.11: Data Arc Time and Length for 3 June

<i>June</i>	<i>Hour</i>	<i>Minute</i>	<i>Obs</i>	$\Delta t$ (s)
3	9	41-42	5	16
	10	2-3	5	16
	10	34-35	5	16
	10	45-46	5	16
	10	56-57	5	16
	11	6-7	5	16
	11	17-18	5	16
	11	28-29	5	16
	11	38-39	4	16
	11	49-50	5	16
	12	0-1	5	16
	12	10-11	5	16
	12	21-22	5	16
	12	32-33	5	16
	12	42-43	5	16
	12	53-54	3	16
	13	4-5	5	16
	13	14-16	5	16
	13	25-26	3	16

and one at the end of the hour. This break in data can be observed in the plots to follow. The data set for 5 June consists of 18 arcs having 5 observations and one arc with 4 observations starting at hour 9 and going through hour 11.

*4.4.1 Data Set 1: 3 – 4 June.* Using the same procedure as that described in Section 4.3, the first step was to run these data arcs through the non-maneuver model. The plots showing right ascension and declination versus time look as though the model produced an accurate solution. See Figure 4.13. The right ascension versus declination plot, however, reveals a slight discrepancy in declination, particularly in the last set of arcs. See Figure 4.14.

The data was then run through the maneuver model using the same method as stated above. Only one maneuver time and state vector completely converged. An initial maneuver time guess between approximately 7 hours and 38 min before and 4

hours after  $t = 80008$  s resulted in convergence on the state vector shown in Table 4.12 with a maneuver time of  $t_m = 80008$  (hour 7, minute 55 on 4 June). Note that

Table 4.12: State Vector Solution for Maneuver Fit to 3-4 June

$\mathbf{X}_0$	$t_m = 80008$
$\delta r$	7229.6
$r_0\delta\theta$	-1.0327e+005
$\delta z$	-25696
$\delta\dot{r}$	0.49347
$r_0\delta\dot{\theta}$	-1.095
$\delta\dot{z}$	-2.1298
$\Delta v_r$	-0.03253
$\Delta v_\theta$	-0.0071178
$\Delta v_z$	0.20463
$\delta t_m$	4.6267e-010

the main component of the maneuver in the state vector solution is in the  $\delta z$ , or n-s direction. This is consistent with a correction in declination.

Figure 4.15 shows right ascension and declination versus time. A slightly better fit to the declination can be seen in the lower plot. A significant improvement, however, is discernable in the right ascension versus declination plot. Figure 4.16 confirms the primary burn in the n-s direction results in a better fit to the second set of data arcs from 4 June. While  $t_m = 80008$  was the only value converged upon for multiple different values of initial maneuver time guesses, it should be noted that numerous single state vector and maneuver time solutions produced reasonable answers. Without convergence, however, there is little confidence that these answers are legitimate solutions.

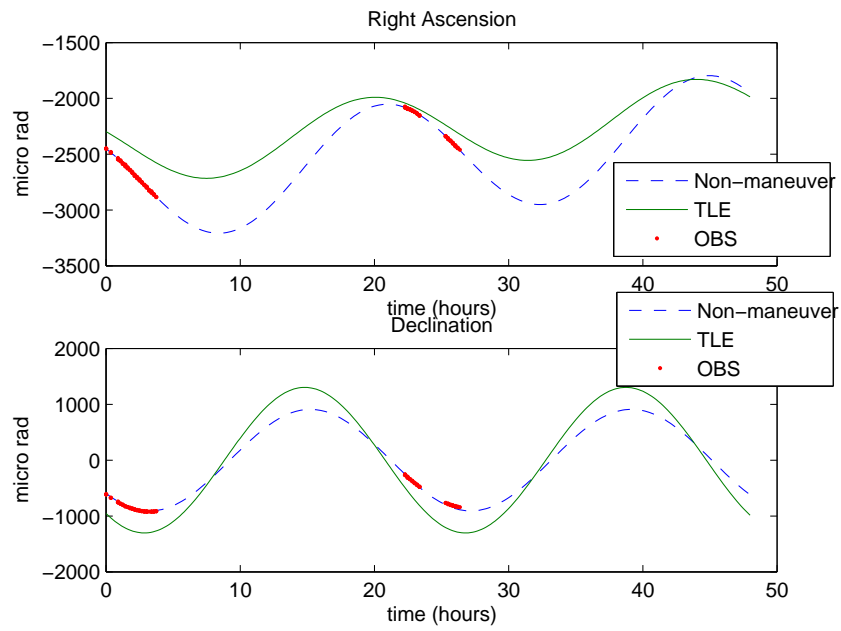


Figure 4.13: Non-maneuver Fit to 3-4 June

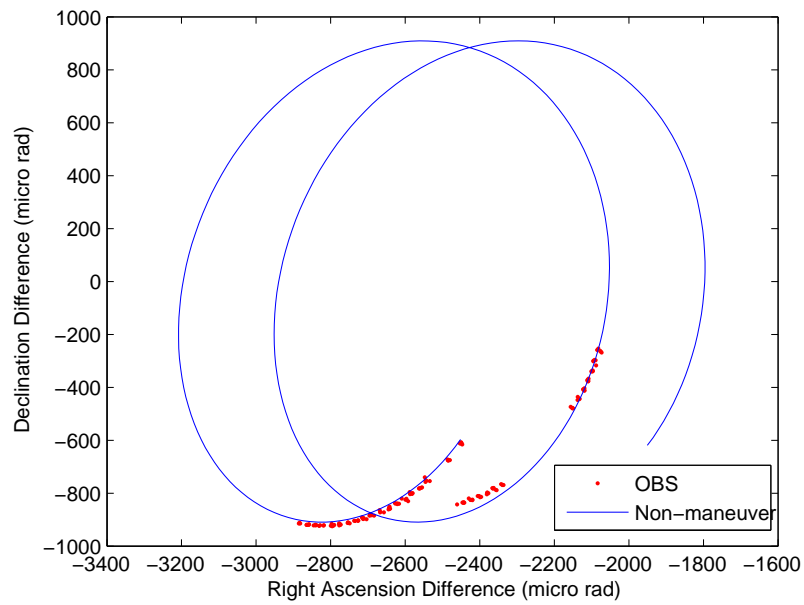


Figure 4.14: Non-maneuver RA vs Dec for 3-4 June

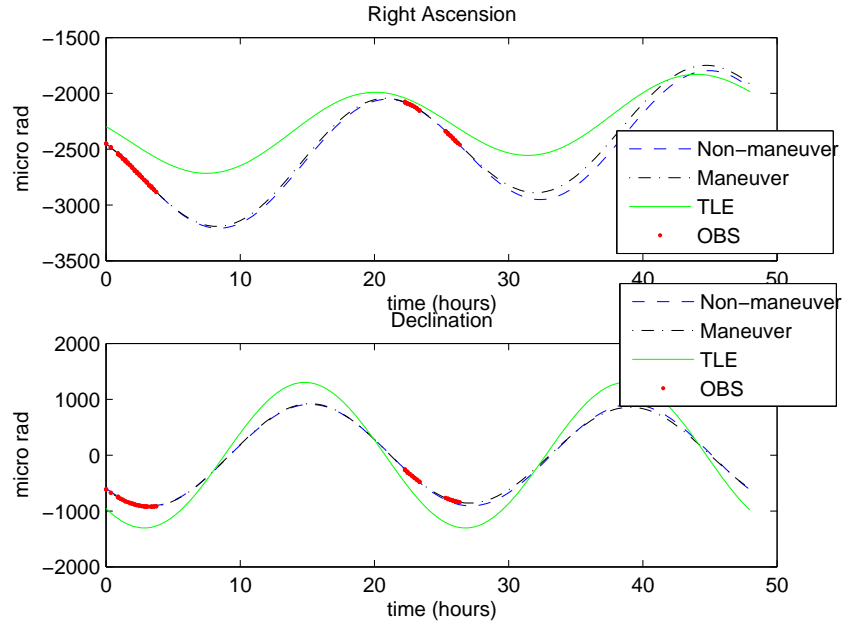


Figure 4.15: Maneuver Fit to 3 – 4 June,  $t_m = 80008$

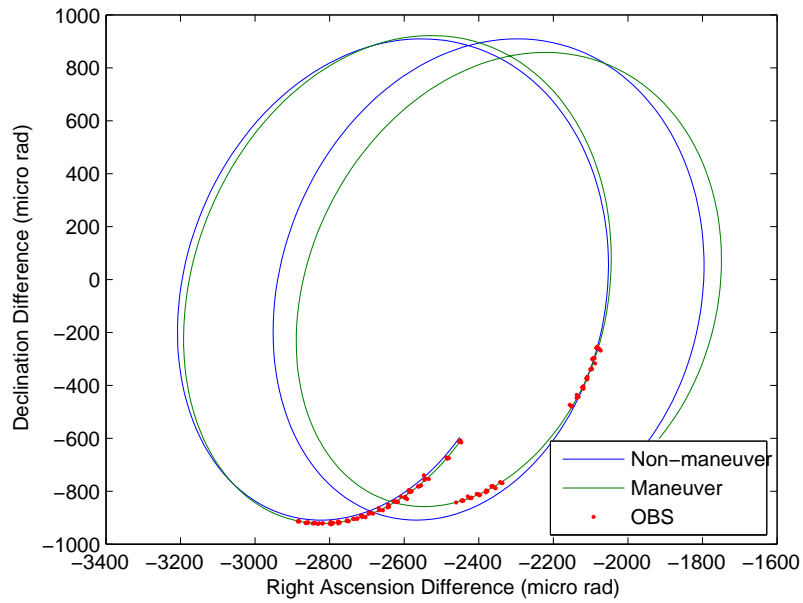


Figure 4.16: RA vs Dec for 3 – 4 June,  $t_m = 80008$

4.4.2 *Data Set 2: 4 – 5 June.* Because the maneuver was suspected between 3 and 4 June, not 4 and 5 June, it would be expected that the solution from the previous section would fit the observations from 5 June if propagated forward for an additional day. As shown in Figure 4.17, this assumption was not validated. The solution for 3 and 4 June did not fit the observations for the 5<sup>th</sup>. Note, however, that

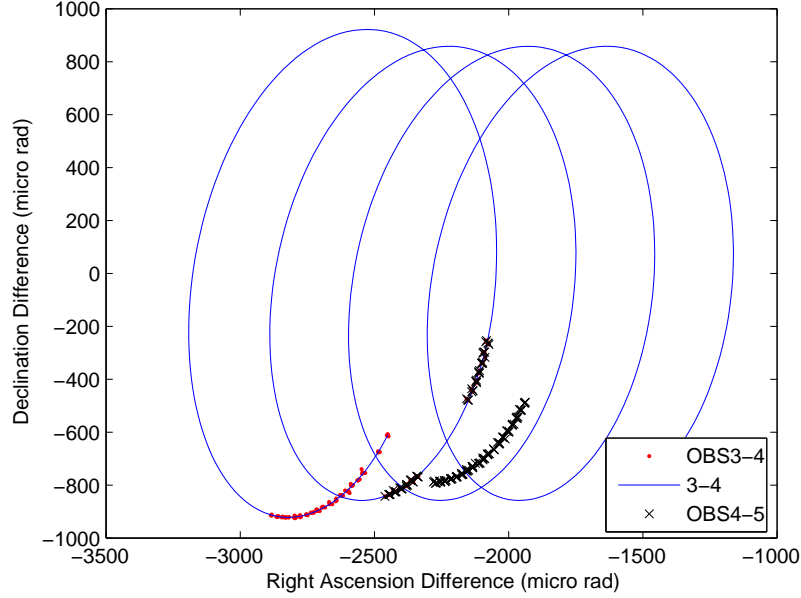


Figure 4.17: RA vs Dec Solution for 3 – 4 June Propagated to 5 June

the change in declination from 4 to 5 June (shown by an upward shift from the second ellipse to the new observations) is equal to the change in declination from 3 to 4 June (shown by an upward shift from the first ellipse to the second ellipse). This would seem to indicate another maneuver.

Due to this discrepancy, it was necessary to revert back to running the data from 4-5 June in the maneuver model. Similar to the previous results, one maneuver time,  $t_m = 87311$ , and state vector solution was converged upon. This solution can be seen in Table 4.13.

As seen in Figure 4.18, not much useful information can be extracted from the plot showing right ascension and declination versus time. Right ascension plotted

Table 4.13: State Vector Solution for Maneuver Fit to 4-5 June

$\mathbf{X}_0$	$t_m = 87311$
$\delta r$	3703.9
$r_0 \delta \theta$	-87686
$\delta z$	-10936
$\delta \dot{r}$	0.66135
$r_0 \delta \dot{\theta}$	-0.57611
$\delta \dot{z}$	-2.5168
$\Delta v_r$	-0.015592
$\Delta v_\theta$	0.005491
$\Delta v_z$	0.21955
$\delta t_m$	1.0763e-011

versus declination, however, reveals the maneuver model solution produced a more accurate fit. This can be seen in Figure 4.19.

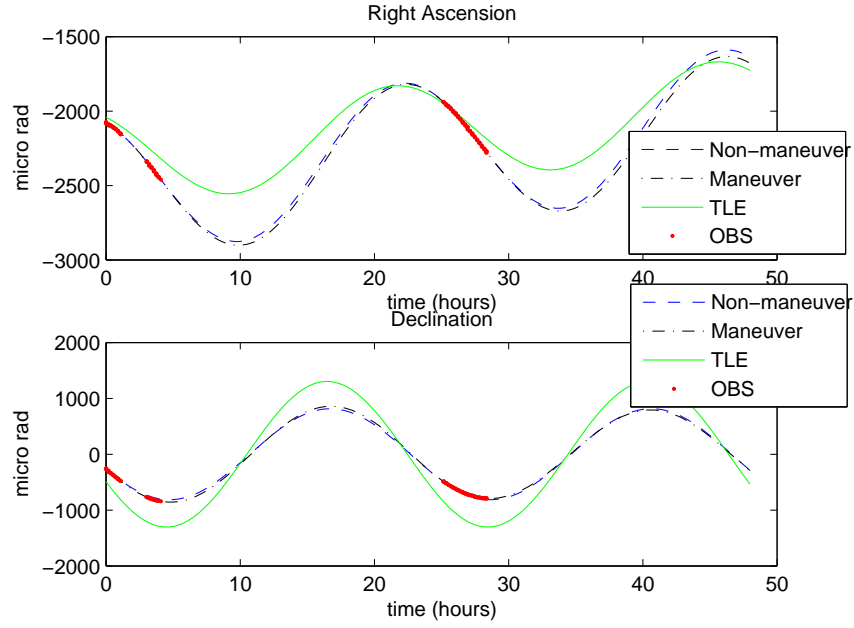


Figure 4.18: Maneuver Fit to 4 – 5 June,  $t_m = 87311$

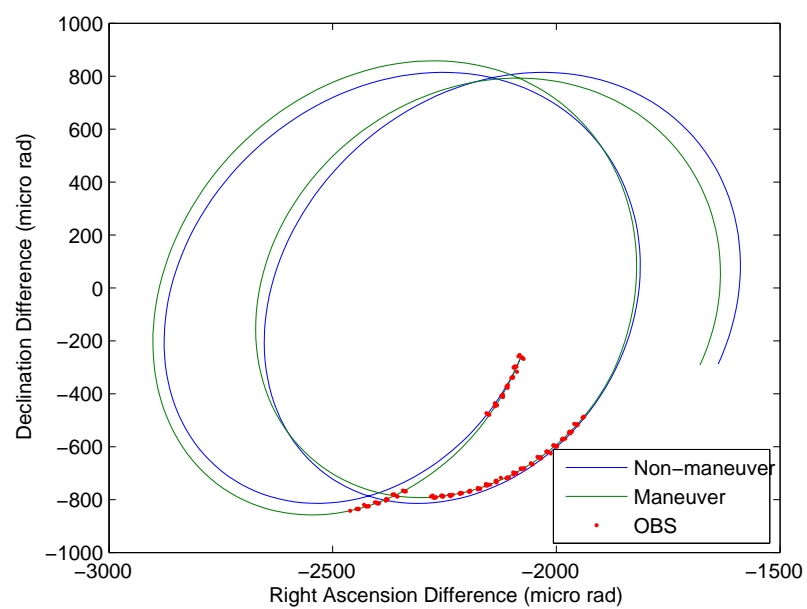


Figure 4.19: RA vs Dec for 4 – 5 June,  $t_m = 87311$

## V. Conclusions

### 5.1 *Summary*

This thesis demonstrates the ability to estimate maneuvers of a collocated satellite in geosynchronous orbit using optical observations and relative orbit determination. Based on the research conducted, it has been found that maneuver estimation has great potential to become a valuable tool in satellite tracking and identification.

### 5.2 *Conclusions*

While this research has demonstrated the potential of maneuver estimation, it did not result in an operationally competent model. Solutions were obtained for three out of four real data sets; however, several issues may be contributing to less than confident results.

*5.2.1 Observability.* Simulation studies with perfect data show that the position, velocity, change in velocity, and time of maneuver can be correctly estimated with a set of observations every ten minutes over the course of an orbit. On the other hand, current amounts of data obtained for tracking satellites have been found to be inadequate. The number of observations obtained for the first data set (29 July – 1 August 2003) generated inconclusive results. The second data set (3 – 5 June 2004), however, was the result of a focused effort specifically designed to obtain more observations. With approximately four times the number of observations, this data set yielded promising results.

This study, therefore, has shown that if maneuver estimation is to be successful, a concentrated effort must be employed and the cluster in question must be given a higher priority so as to obtain more observations than that necessary to track a regular satellite. The level of observability required to accurately estimate maneuvers in GEO is far greater than the current methodology employed to simply track satellites or clusters of satellites. Obtaining one or two arcs of data each hour for three to four hours has been shown to be inadequate.



*5.2.2 Higher Order Error Sources.* Another contribution to the inconclusive maneuver results produced with running the real data in the maneuver model is higher order error sources. If not monitored, small errors can build up and significantly alter a satellite's orbit, thus requiring frequent updates to the orbit determination prediction. Combined with a relatively small number of observations over the course of an orbit, error sources such as coordinate system errors, solar radiation pressure, and other unmodeled dynamics could serve to inhibit convergence within the model.

*5.2.3 Sequential Maneuvers.* As mentioned in Section 4.4.2, sequential maneuvers are also a possibility. Due to the recent developments in propulsion technology many companies are moving towards the use of electric, or ion, thrusters. Ion thrusters produce a higher specific impulse, or Isp, than their chemical counterparts, allowing for a reduction in propellant mass and an increase in satellite lifetime [2]. This higher Isp usually equates to lower thrust which may lead to an increase in the number of burns required for stationkeeping. The increased efficiency of these thrusters, however, make maneuvers on successive days a possibility.

### **5.3 Future Work**

Given the conclusions above, there are several areas of additional research which would benefit the maneuver estimation process.

One such area is to study the effects of small errors to include solar radiation pressure and other unmodeled dynamics, coordinate system errors, and higher order stationkeeping perturbations. By systematically isolating different potential error sources it may be possible to quantify the effects of these errors.

Another area of research involves determining the amount of data required to obtain a confident solution. This would also include evaluating observation quantities and available optical assets versus necessary optical assets across the globe.

Given the increased use of ion thrusters, the possibility of multiple maneuvers within a data set should be investigated.

Finally, *a priori* information on actual stationkeeping maneuvers, as well as satellite capabilities, would greatly assist in the model validation process. This would involve establishing working relationships with satellite owners and operators.

## Bibliography

1. Abbot, R.I., et al. *Close Geostationary Satellite Encounter Analysis: 1997-2001*. Conference Proceedings, AAS 98-118, AAS/AIAA Space Flight Mechanics Meeting San Antonio, TX, January 2002.
2. Boeing. *Xenon Ion Propulsion*. Boeing Satellite Systems Inc., 2005. <http://www.boeing.com/defense-space/space/bss/factsheets/xips/xips.html>.
3. Chao, C.C., et al. *Ground Tracking and Control of GEO Cluster Satellites Using The Raven Telescope*. Conference Proceedings, AAS 01-165, AAS/AIAA Space Flight Mechanics Meeting, Santa Barbara, CA, February 2001.
4. Gist, R.G. and D.L. Oltrogge. *Risk Management Of Unintentionally Collocated Geosynchronous Spacecraft*. Conference Proceedings, AAS 01-321, AAS/AIAA Astrodynamics Specialist Conference Quebec City, Canada, August 2001.
5. Hill, K., et al. *Relative Orbit Determination of Geosynchronous Satellites Using the COWPOKE Equations*. Conference Proceedings, AAS 04-195, AAS/AIAA Space Flight Mechanics Meeting, Maui, HI, February 2004.
6. Hoots and Roehrich. *SpaceTrack Report No. 3*. Technical Report, Peterson AFB, CO: Aerospace Defense Center, December 1980. <http://celestrak.com/NORAD/documentation/spacetrk.pdf>.
7. Kelso, T.S. *Basics of the Geostationary Orbit*. Celestrak, 1998. <http://celestrak.com/columns/v04n07>.
8. Mueller, Ivan I. *Spherical and Practical Astronomy as Applied to Geodesy* (First Edition). New York, NY: Frederick Ungar Publishing CO., 1969.
9. Pattinson, Lindsay and Vladimir Chechik. *EUTELSAT Satellite Collocation*. Conference Proceedings, AAS 01-317, AAS/AIAA Astrodynamics Specialist Conference Quebec City, Canada, August 2001.
10. Sabol, C., et al. "Satellite Formation Flying Design and Evolution," *Journal of Spacecraft and Rockets*, Vol. 38(No. 2) (March-April 2001).
11. Sabol, C., et al. *Analysis of the Telstar-401/GOES-10 Close Approach Using the Raven Telescope*. Conference Proceedings, AAS 98-118, AAS/AIAA Space Flight Mechanics Meeting Monterey, CA, February 1998.
12. Sabol, C., et al. *Recent Developments of the Raven Small Telescope Program*. Conference Proceedings, AAS 02-131, AAS/AIAA Space Flight Mechanics Meeting, San Antonio, TX, January 2002.
13. Sabol, C., et al. *Meet the Cluster Orbits With Perturbations Of Keplerian Elements (COWPOKE) Equations*. Conference Proceedings, AAS/AIAA Space Flight Mechanics Meeting, Ponce, Puerto Rico, February 2003.

14. Sauer, B. and M. Chow. *Geosynchronous Satellite Collocation at Space Systems/Loral*. Conference Proceedings, AAS 01-319, AAS/AIAA Astrodynamics Specialist Conference Quebec City, Canada, August 2001.
15. Vallado, David A. *Fundamentals of Astrodynamics and Applications* (First Edition). New York, NY: McGraw-Hill Companies, Inc., 1997.
16. Wiesel, William E. *Spaceflight Dynamics* (Second Edition). Boston, MA: Irwin McGraw-Hill, 1997.
17. Wiesel, William E. *Modern Orbit Determination* (First Edition). Beavercreek, OH: Aphelion Press, 2003.

<b>REPORT DOCUMENTATION PAGE</b>					<i>Form Approved</i> <b>OMB No. 0704-0188</b>	
The public reporting burden for this collection of information is estimated to average 1 hour per response, including the time for reviewing instructions, searching existing data sources, gathering and maintaining the data needed, and completing and reviewing the collection of information. Send comments regarding this burden estimate or any other aspect of this collection of information, including suggestions for reducing this burden to Department of Defense, Washington Headquarters Services, Directorate for Information Operations and Reports (0704-0188), 1215 Jefferson Davis Highway, Suite 1204, Arlington, VA 22202-4302. Respondents should be aware that notwithstanding any other provision of law, no person shall be subject to any penalty for failing to comply with a collection of information if it does not display a currently valid OMB control number. <b>PLEASE DO NOT RETURN YOUR FORM TO THE ABOVE ADDRESS.</b>						
<b>1. REPORT DATE</b> (DD-MM-YYYY) 21-03-2005		<b>2. REPORT TYPE</b> Master's Thesis			<b>3. DATES COVERED</b> (From — To) Sep 2003 — Mar 2005	
<b>4. TITLE AND SUBTITLE</b>  Maneuver Estimation Model for Relative Orbit Determination					<b>5a. CONTRACT NUMBER</b>  <b>5b. GRANT NUMBER</b>  <b>5c. PROGRAM ELEMENT NUMBER</b>  <b>5d. PROJECT NUMBER</b>  <b>5e. TASK NUMBER</b>  <b>5f. WORK UNIT NUMBER</b>  	
<b>6. AUTHOR(S)</b>  Storch, Tara R., Capt, USAF					<b>8. PERFORMING ORGANIZATION REPORT NUMBER</b>  AFIT/GA/ENY/05-M011	
<b>7. PERFORMING ORGANIZATION NAME(S) AND ADDRESS(ES)</b> Air Force Institute of Technology Graduate School of Engineering and Management 2950 Hobson Way WPAFB OH 45433-7765					<b>10. SPONSOR/MONITOR'S ACRONYM(S)</b>  <b>11. SPONSOR/MONITOR'S REPORT NUMBER(S)</b>  	
<b>9. SPONSORING / MONITORING AGENCY NAME(S) AND ADDRESS(ES)</b> AFRL Det 15 Attn: Dr. Chris Sabol 535 Lipoa Pkwy, Ste 200 Kihei, HI 96753 808-874-1594					<b>12. DISTRIBUTION / AVAILABILITY STATEMENT</b>  Approval for public release; distribution is unlimited.	
<b>13. SUPPLEMENTARY NOTES</b>						
<b>14. ABSTRACT</b>  This research investigated relative orbit determination of individual satellites within a cluster, focusing on instances when a maneuver has been detected or suspected. Developed using non-linear least squares estimation, the maneuver model estimates magnitude, direction, and time of a suspected maneuver. Observations for the DirecTV 4S and AMC-4 satellite collocation were obtained from the Air Force Maui Optical and Supercomputing (AMOS) site consisting of differential right ascension and declination. Dynamics are modeled using Hill's equations.						
<b>15. SUBJECT TERMS</b>  Relative Orbit Determination, Collocation, Maneuver						
<b>16. SECURITY CLASSIFICATION OF:</b>			<b>17. LIMITATION OF ABSTRACT</b>		<b>18. NUMBER OF PAGES</b>	
a. REPORT	b. ABSTRACT	c. THIS PAGE	UU		77	
U	U	U	<b>19a. NAME OF RESPONSIBLE PERSON</b> William E. Wiesel, USAF (ENY)			
						<b>19b. TELEPHONE NUMBER</b> (include area code) (937) 255-3636, ext 4312